Research article

A numerical approach to optimize the performance of HTL-free carbon electrode-based perovskite solar cells using organic ETLs

Sumbel Ijaz [a], Ehsan Raza [b], Zubair Ahmad [b,*], Haris Mehmood [a], Muhammad Zubair [c,****], Muhammad Qasim Mehmood [a,**], Yehia Massoud [c,***]

[a] *Department of Electrical Engineering, Information Technology University of the Punjab (ITU), 54000 Lahore, Pakistan*
[b] *Qatar University Young Scientists Center (QUYSC), Qatar University, 2713, Doha, Qatar*
[c] *Innovative Technologies Laboratories (ITL), King Abdullah University of Science and Technology (KAUST), Thuwal, 23955, Saudi Arabia*

ARTICLE INFO

ABSTRACT

Carbon electrode-based perovskite solar cells (c-PSCs) without a hole transport layer (HTL) have obtained a significant interest owing to their cost-effective, stable, and simplified structure. However, their application is limited by low efficiency and the prevalence of high-temperature processed electron transport layer (ETL), e.g. TiO_2, which also has poor optoelectronic properties, including low conductivity and mobility. In this study, a series of organic materials, namely PCBM ((Park et al., 2023; Park et al., 2023) [6,6]-phenyl-C61-butyric acid methyl ester, C72H14O2), Alq_3 ($Al(C_9H_6NO)_3$), BCP (2,9-Dimethyl-4,7-diphenyl-1,10-phenanthroline, $C_{26}H_{20}N_2$), C_{60}, ICBA (indene-C60 bisadduct, $C_{78}H_{16}$) and PEIE (poly (ethylenimine) ethoxylated, $(C_{37}H_{24}O_6N_2)_n$) have been numerically analyzed in SCAPS-1D solar simulator to explore alternative potential ETL materials for HTL-free c-PSCs. The presented device has FTO/ETL/$CH_3NH_3PbI_3$/carbon structure, and its performance is optimized based on significant design parameters. The highest achieved PCEs for PCBM, Alq_3, BCP, C_{60}, ICBA, and PEIE-based devices are 22.85%, 19.08%, 20.99%, 25.51%, 23.91%, and 22.53%, respectively. These PCEs are obtained for optimum absorber thickness for each case, with an acceptor concentration of 1.0×10^{17} cm^{-3} and defect density of 2.5×10^{13} cm^{-3}. The C_{60}-based cell has been found to outperform with device parameters as V_{oc} of 1.29 V, J_{sc} of 23.76 mA/cm^2, and FF of 82.67%. As the design lacks stability when only organic materials are employed, each of the presented devices have been analyzed by applying BiI_3, LiF, and ZnO as protective layers with the performances not compromised. We believe that our obtained results will be of great interest in developing stable and efficient HTL-free c-PSCs.

 * Corresponding author.
 ** Corresponding author.
 *** Corresponding author.
 **** Corresponding author.
  E-mail addresses: zubairtarar@qu.edu.qa (Z. Ahmad), muhammad.zubair.3@kaust.edu.sa (M. Zubair), qasim.mehmood@itu.edu.pk (M.Q. Mehmood), yehia.massoud@kaust.edu.sa (Y. Massoud).

1. Introduction

Photovoltaic (PV) cells have earned worldwide significance as a sustainable and potential technology to realize energy needs because of their continuously improving performance, environmental friendliness, massive production, and low manufacturing cost compared with fossil fuels. Conventional silicon-based solar cells have reached maturity featured with merits and demerits in that they have higher efficiencies and longer lives but their massive production is not supportive due to complex and expensive fabrication techniques [1]. Organic-inorganic hybrid perovskites have been replacing them because of their tremendous progress during the last decade [2,3]. Perovskites were first used in PV cells in 2009 [4,5] and demonstrated an efficiency of 3.8%. Recently, Perovskite Solar Cells (PSCs) have successfully reached a cell efficiency of 26.08% (certified 25.73%) [6], which is very close to that of the crystalline-silicon cells conversion efficiency of 26.7% [7]. They have been able to procure a tremendous and escalating interest because of their counting factors towards success, such as low processing cost, wideband absorption with absorption coefficient as high as $>10^{-4}$ cm^{-1}, tunable electro-optical bandgap [8], superconductivity, long transport length of charge carriers, good charge mobility ($\sim$10 cm^2 V^{-1}s^{-1}), quick separation of charges and a low exciton binding energy ($<$100 meV) [9].

To explore and to realize improved device performance, a number of configurations, including mesoporous [10], planar hetero-junction, hole transport layer (HTL)-free [11], and the electron transport layer (ETL)-free structures [12] have so far been presented. In a mesoporous perovskite structure, a mesoporous metal oxide is coated with sensitizer, whereas in a planar configuration, the fabrication is simpler because of being free from high-temperature sintering. A sound solar cell engineering combines materials favorable optical absorption characteristics and exceptional charge-transport properties [13]. In a most conventional scheme, a PSC is composed of transparent conducting oxide/ETL/Perovskite/HTL/back metal layer where back contact is made of noble metals making the overall device design complicated and expensive. Also, spiro-OMeTAD [14], which is the most widely used HTL in highly efficient PSCs, but, it is costly and has instability issues, it raises the overall device cost which impedes its commercialization. In addition, HTL is one of the significant reasons for device degradation; hence, consistent efforts have shifted toward HTL-free devices [11,15]. In this regard, carbon electrode-based perovskite solar cells (c-PSCs) without HTL [16] have been considered an alternative with acceptable performance, excellent stability, simple fabrication, and reduced cost.

Carbon is a promising alternative in HTL-free structures as back metal contact due to its good electrical conductivity and chemical stability [17]. Despite its low-cost and excellent stability, the efficiency in these structures is lower than that of PSCs with HTL and having metals as back contacts. However, these cells had not very impressive starting efficiencies, i.e. 6.6% [16], later on compositional engineering and use of novel fabrication techniques improved efficiencies over 18% [18]. In addition, device efficiencies of 20.43% and over 25% have also been realized by employing simulation studies [19,20]. With the maximum theoretical Shockley-Queisser (S-Q) limit standing above 30% for single junction solar cells [21], avenues are still wide open for research in this domain to explore better, more efficient, and cost-effective configurations [22].

The performance of HTL-free devices is even more dependent on ETL materials because they offer charge extraction while simultaneously blocking holes [23]. A good ETL material has a transparent spectrum in the UV–Vis region, and its lowest unoccupied molecular orbital (LUMO) and highest occupied molecular orbital (HOMO) levels are higher than that of the absorber layer. The conventionally used ETL, i.e. TiO$_2$ poses challenges, such as the need for high annealing temperature making it incompatible with flexible substrates. In addition, the hysteresis challenge arises when used in the planar configuration. Therefore, to come up with alternative potential ETLs, a set of different ETL materials, either inorganic or organic, with their associated benefits, have been used for device design. As nearly half of the solar energy lies in the near-infrared (NIR) region, the research focuses on NIR PV materials. Organic semiconductors are the ideal candidates for this role as their absorption is tunable based on their molecular engineering. They have lower cost, simple synthetic protocols, environmental friendliness, tunable optoelectronic properties, and mechanical flexibility and are available in abundance, getting popular as ETLs in currently designed cells [24]. Therefore, it has become crucial to expand research related to organic materials to assess design concepts that can build on their associated advantages.

In this work, we have employed the One-Dimensional Solar Cell Capacitance Simulator (SCAPS-1D) laid out by the University of Gent [25] to analyze the effect of varying device parameters on the performance of presented devices. The design under study is
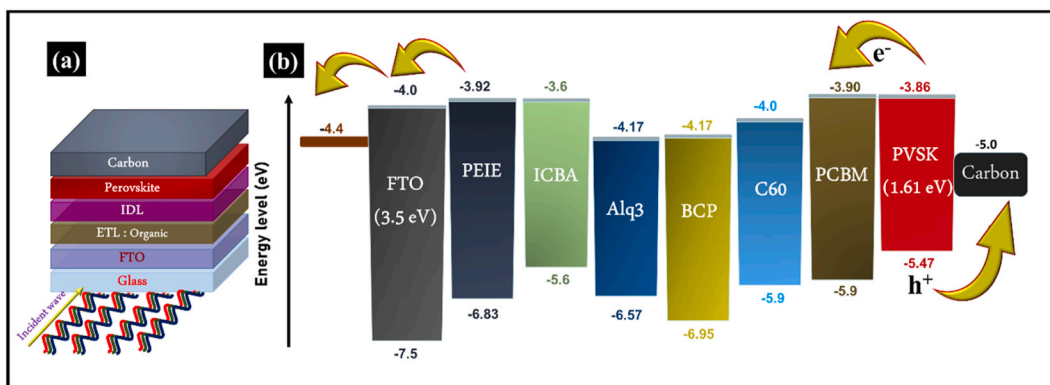

Fig. 1. (a) The HTL-free Perovskite solar cell device with organic ETL materials and (b) the associated energy level diagram.

carbon-based HTL-free PSC with different organic ETL materials, including PCBM, Alq$_3$, BCP, C$_{60}$, ICBA, and PEIE [26]. The motivation behind proceeding this study is to conduct a comparative analysis in order to investigate the best alternative potential ETLs for a perovskite solar cell. The designs are evaluated in terms of their J-V characteristics, FFs, PCEs, and QEs. The designs have been optimized for their performances using thicknesses of various layers, donor density (N$_D$), acceptor density (N$_A$), defect density (N$_t$), carrier mobility (μ), carrier diffusion lengths (L$_n$, L$_p$), and carrier lifetime (τ$_n$, τ$_p$). The highest achieved PCEs for PCBM, Alq$_3$, BCP, C$_{60}$, ICBA, and PEIE-based devices are 22.85%, 19.08%, 20.99%, 25.51%, 23.91%, and 22.53%, respectively, when each of them had an optimum value of layer thickness with defect density equal to 2.5×10^{13} cm^{-3} and N$_A$ was equal to 10^{17} cm^{-3}. The C$_{60}$-based cell has been found to outperform with V$_{oc}$ of 1.29 V, J$_{sc}$ of 23.76 mA/cm^2, and FF of 82.67%. Further, as the devices with organic materials are prone to stability issue, which has been tackled using protective layers of BiI$_3$ [27], ZnO [28], and LiF [29,30], without affecting the device efficiencies.

2. Simulation and device modelling

A uniformly doped metal-halide perovskite (CH$_3$NH$_3$PbI$_3$) based device in HTL-free configuration has been employed for this study. The device is an HTL-free hetero-junction cell with a layer configuration of Carbon/absorber layer (CH$_3$NH$_3$PbI$_3$)/Interface Defect Layer (IDL)/(ETL (only organic))/FTO (Fluorine-doped Tin Oxide) as depicted in Fig. 1 (a). The transparent conducting oxide, i.e., FTO, is employed as the front contact, and carbon with a work function close to gold is used here as the back contact. At the same time, a thin IDL is present for seeing the impact of interfacial charge recombination. The top contact must ideally be highly transparent having minimal electrical losses. In this study, we have optimized the cell performance by employing six different organic ETL materials. The energy level diagram for the materials under investigation is included in Fig. 1 (b). The device design parameters are taken from the literature and are listed in Table 1, while the defect parameters of layers are kept the same as those in Refs. [31,32]. Thermal velocities of both electron and hole are set to 1×10^7 cm/s. The defect energy level (E$_g$) center is of neutral defect type; the Energy distribution is Gaussian with 0.1 eV characteristic energy. The Capture cross section for both the electron and hole is 2×10^{-14} cm^2. The work functions for left and right contacts are 4.4 eV (FTO) and 5.0 eV (Carbon), respectively. The device is studied under AM 1.5 illumination at an operating temperature of 298.16 K. The potentials, current densities, fill factor, and power conversion efficiency under different parameter optimization are studied.

2.1. Selection of ETL materials

In the design of PSCs, ETL selection is critical for successful device operation, as it facilitates electron transfer and blocks holes; thus, its electron mobility should be high. The Conduction Band Offset (CBO) of ETL and absorber layer plays a significant role in performance determination. In general, its negative values mean smaller interfacial recombination activation energy, resulting in lower V$_{oc}$ and PCE values. However, its positive value leads to a larger activation energy of interface recombination, higher V$_{oc}$ and PCEs [44]. Here, we have compared the performance of the HTL-free device by employing six different organic materials, including PCBM (C72H14O2 [6,6],-phenyl-C61-butyric acid methyl ester), Alq$_3$ (Al(C$_9$H$_6$NO)$_3$), BCP (2,9-Dimethyl-4,7-diphenyl-1,10-phenanthroline, C$_{26}$H$_{20}$N$_2$), C$_{60}$, ICBA (indene-C60 bisadduct, C$_{78}$H$_{16}$) and PEIE (poly-ethylenimine ethoxylated, (C$_{37}$H$_{24}$O$_6$N$_2$)$_n$) as the ETL whose chemical formations are shown in Fig. 2. The CBO values of the corresponding materials are included in Table 2 with initially obtained performances without optimization.

Table 1
Device simulation parameters of each layer for the proposed device.

	FTO	IDL	Perovskite	PCBM	Alq$_3$	BCP	C$_{60}$	ICBA	PEIE
Layer Thickness (nm)	300	5	800 (Variable)	20	20	20	20	20	20
E$_g$: Bandgap (eV)	3.5	1.610	1.610	2.0	2.8	2.78	1.9	2.0	2.91
χ: Electron Affinity (eV)	4	3.86	3.86	3.9	4.17	4.17	4.0	3.6	3.92
ε$_r$: Relative Permittivity	9	6.5	6.5	3.9	3.4	2.7	10	3.825	3.065
N$_c$: Effective density of states for Conduction band (cm^{-3})	2.2×10^{18}	1.0×10^{17}	1.0×10^{17}	2.5×10^{21}	1.44×10^{20}	6×10^{21}	8×10^{19}	5×10^{18}	2.8×10^{19}
N$_v$: Effective density of states for Valence band (cm^{-3})	1.8×10^{19}	1.0×10^{17}	1.0×10^{17}	2.5×10^{21}	1.44×10^{20}	6×10^{21}	8×10^{19}	5×10^{18}	1.04×10^{19}
μ$_n$: Mobility of electron (cm^2/Vs)	20	2.0	2.0	0.2	1.9×10^{-5}	1.1×10^{-3}	8×10^{-2}	6.9×10^{-3}	1×10^{-3}
μ$_p$: Mobility of fole (cm^2/Vs)	10	2.0	2.0	0.2	2×10^{-7}	5×10^{-6}	3.5×10^{-6}	6.9×10^{-3}	1×10^{-5}
N$_A$: Acceptor concentration (cm^{-3})	0	1×10^{13}	1×10^{13} (Variable)	0	–	–	–	–	–
N$_D$: Donor concentration (cm^{-3})	2×10^{19}	0	0	1×10^{21}	1×10^{21}	1×10^{21}	1×10^{21}	1×10^{21}	1×10^{19}
N$_t$: Defect Density (cm^{-3})	1×10^{16}	1×10^{16}	2.5×10^{13} (Variable)	1×10^{13}	1.3×10^{17}	2×10^{18}	$2.6\ 10^{18}$	1.3×10^{15}	2.5×10^{17}
Reference	[33]	[33–35]	[31]	[36]	[37,38]	[39]	[40]	[41]	[42,43]
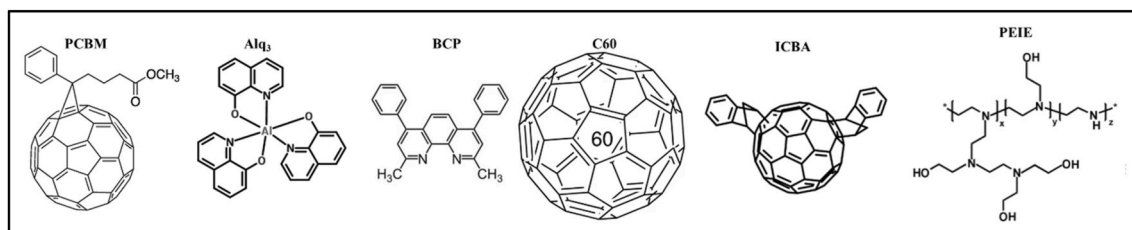
Fig. 2. Chemical structures of PCBM, Alq₃, BCP, C₆₀, ICBA, and PEIE, used as ETL materials.

Table 2
The performance parameters of solar cells after initial optimization with device parameters listed in Table 1 and conduction band offsets (CBOs) for different ETL materials where the electron affinity (χ) for the absorber layer is taken to be 3.86 eV.

Electron transport layer	V_{oc} (V)	J_{sc} (mA/cm²)	FF (%)	PCE (%)	Electron affinity of ETL	CBO =(χ_pvsk – χ_ETL) (eV)
PCBM	0.897828	26.01866	73.0499	17.0647	3.9	−0.04
Alq₃	1.118256	23.92755	68.9558	18.4506	4.17	−0.31
BCP	1.01986	23.77683	63.7424	15.4569	4.17	−0.31
C₆₀	1.024168	26.03656	71.142	18.9706	4.00	−0.14
ICBA	1.12334	23.81859	81.2271	21.7335	3.6	0.26
PEIE	1.1238	23.99618	76.6305	21.84255	3.92	−0.06

Fig. 3. The device performance variation for absorber thickness (400–2000 nm), (a) V_{oc} (V), (b) J_{sc} (mA.cm⁻²), (c) FF (%), and (d) PCE (%).

3. Results and discussion

By making the previously presented work in Ref. [31] a baseline where all ETLs were inorganic, here the design performance is evaluated with organic ETL materials. For the presented design, the FTO layer has a thickness of 300 nm, each ETL material is set to have a thickness of 20 nm, the active l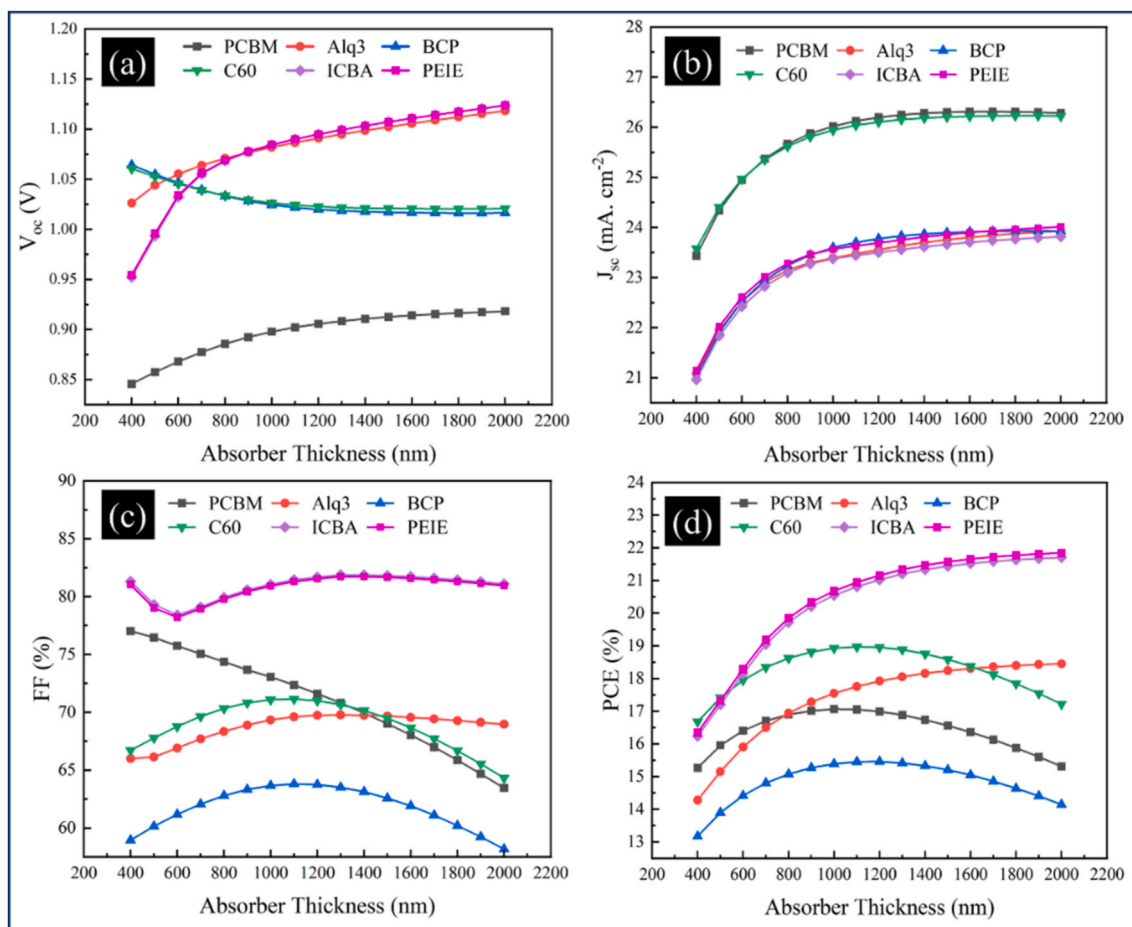ayer has variable thickness for optimum performance, and the IDL is 5 nm thick. A thicker ETL leads to a higher series resistance limiting the photo generation, which in turn causes a decrease in J_{sc} and hence in overall cell efficiency. This study encompasses many significant performance-affecting analyses, including charge mobility and carrier diffusion length of $CH_3NH_3PbI_3$, doping concentration, defect density, operating temperature, and back metal contact work function. In solar cells, after the light-harvesting and electron-hole pair generation processes, electrons often want to return to their stable state in the valence band. This phenomenon generally lead to dissipation resulting from the recombination process. Recombination processes can be classified into numerous groups [45]. Recombination processes generally take place via radiative, Auger, and Shockley-Read-Hall (SRH) mechanisms. Radiative recombination occurs when an electron from the conduction band combines with a hole from the valence band, resulting in the emission of a photon within the bandgap region. Auger recombination happens when the released energy or photon is transported to another free charge carrier (electron or hole) through a precise approach.

3.1. Effect of absorber layer thickness

The MAPbI$_3$ device is first optimized for absorber thickness, a significant performance descriptor in a PSC [46], as each performance parameter is sensitive to it. When light is illuminated, electron-hole pair generation occurs inside the absorber layer, eventually giving rise to voltage generation after their collection at the cathode and anode. The device under study is analyzed under the change of absorber thickness between 400 nm and 2000 nm to see its impact. The resulting variation in photovoltaic parameters is plotted in Fig. 3(a–d), where it can be seen that there is an optimum thickness for each of the devices. A thicker absorber, though, leads to increased performance but only before a particular value i.e. is the optimum thickness value for a given structure as recombination
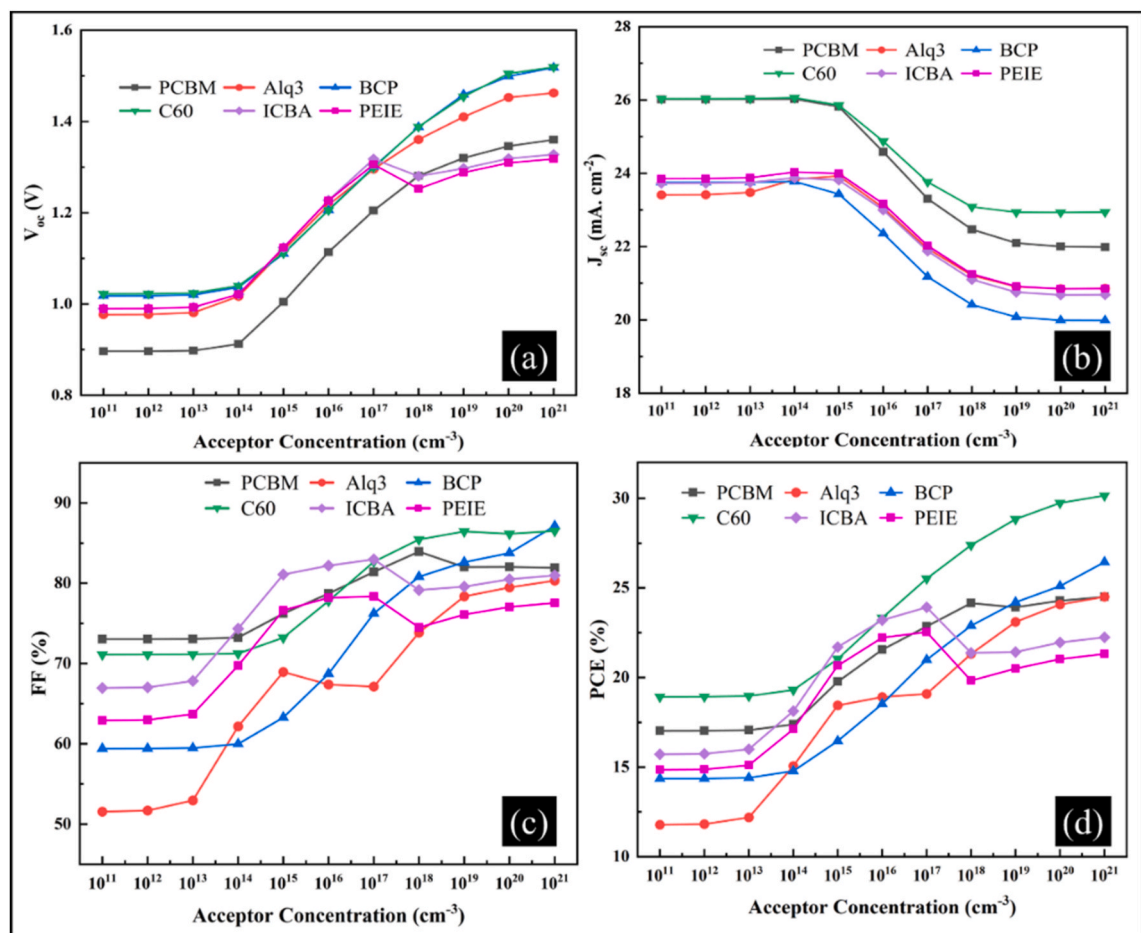

Fig. 4. The change in performance parameters of PSC with N_A from 10^{11} to 10^{21} cm^{-3} for different ETL materials (a) V_{oc} (V), (b) J_{sc} (mA.cm^{-2}), (c) FF (%), and (d) PCE (%).

starts to increase beyond that. The value of optimum absorber thickness for PCBM is 1000 nm; for Alq$_3$ it is 2000 nm; for BCP it is 1200 nm; for C$_{60}$ it is 1100 nm; for ICBA and PEIE it is 2000 nm with the highest of efficiencies being 17.06%, 18.45%, 15.45%, 18.97%, 15.40%, 21.702%, and 20.665% respectively. J$_{sc}$ increases with absorber thickness initially, but the increase proportion reduces after saturation. In addition, some of the materials have shown relatively inefficient charge separation and poorer transport of charges, resulting in a low photocurrent generation. V$_{oc}$ increases in many cases due to increased absorption, which causes a large number of photo-generated carriers and increases the built-in electric field; however, the decrease in V$_{oc}$ is observed in BCP and C$_{60}$ materials with increasing thickness due to the increased recombination rate. FF decreases after a certain value for most cases, which is attributed to an increased value of series resistance. In addition, a thick absorber may pose fabrication challenges and raise electrical losses.

3.2. Effect of acceptor concentration (N$_A$)

The device performance greatly depends on the acceptor density (N$_A$) of the holes in the active layer, as the performance of a semiconductor device improves with doping through increased electric field strength. In this work, the value of N$_A$ for MAPbI$_3$ layer is varied from 10^{11} to 10^{21} cm^{-3}. As N$_A$ increases, the width of the depletion layer decreases, which increases the neutral region size, and hence the bulk recombination occurs. It can be seen from Fig. 4 (a) that V$_{oc}$ increases due to the charge separation towards corresponding electrodes [20]. This increase in voltage is also attributed to a decreased holes fermi level. Fig. 4 (b) shows that J$_{sc}$ starts decreasing beyond 10^{15} cm^{-3} after remaining constant due to Auger recombination which becomes more significant at higher N$_A$. The PCE is high at larger N$_A$ values where its highest values are realized for N$_A = 10^{21}$ cm^{-3} as 24.49%, 24.50%, 26.43%, and 30.15% for PCBM, Alq$_3$, BCP, C$_{60}$, cases respectively. However, the optimum values for ICBA and PEIE are observed to be N$_A = 10^{17}$ cm^{-3}. The overall highest performance is realized with C$_{60}$ because it improves cell performance with exceptional electron mobility and electron-accepting properties.
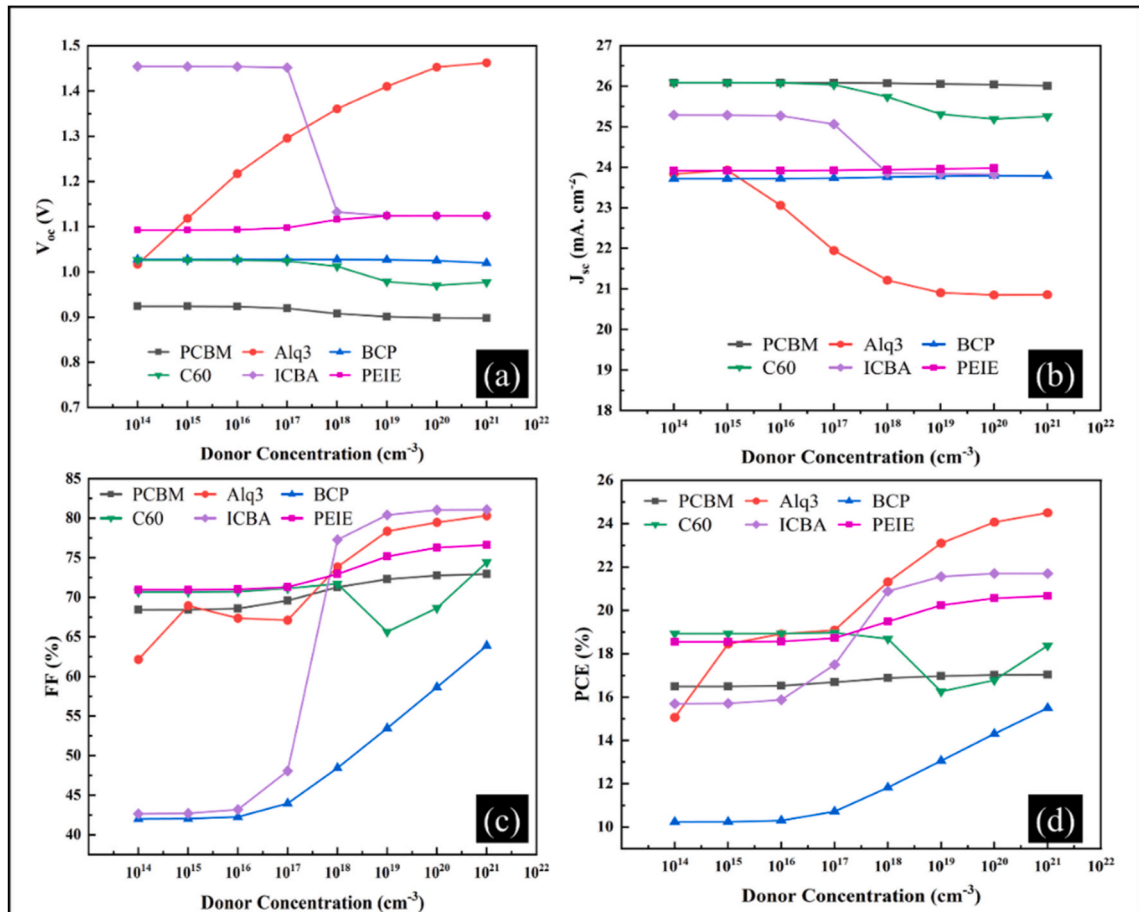

Fig. 5. Variation of device performance parameters (a) V$_{oc}$ (V), (b) J$_{sc}$ (mA/cm^2), (c) FF (%) and (d) PCE (%) with the change of donor concentration (N$_D$) for each ETL from 10^{14} to 10^{21} cm^{-3}.

3.3. Effect of ETL donor concentration (N_D)

For best output parameters, the donor concentration (N_D) of each ETLs also needs optimization. It has its significance in the performance evaluation of the device. N_D has been varied from 10^{14} to 10^{21} cm^{-3} for each ETL case. It can be seen from Fig. 5(a–d) that in most of the cases, the performance is higher when N_D has larger values. The peak values of PCEs achieved for $N_D = 10^{21}$ cm^{-3} are 17.02%, 24.50%, 15.49%, 21.70%, and 20.66% for PCBM, Alq$_3$, BCP, ICBA, and PEIE, respectively. However, the highest value of PCE of 18.97% was achieved for 10^{17} cm^{-3} for the C$_{60}$ case. Similarly, the highest values for FF are obtained when N_D is 10^{21} cm^{-3} as 72.94%, 80.32%, 63.90%, 74.45%, 81.09%, and 76.63% for PCBM, Alq$_3$, BCP, C$_{60}$, ICBA, and PEIE, respectively. The improved charge transport and decreased recombination at high values of ETM's N_D lead to enhanced device performance. However, an increase in N_D beyond a specific value may reduce the device efficiency because of an increase in carrier trapping.

3.4. Effect of defect-density (N_t) of CH$_3$NH$_3$PbI$_3$ layer

The absorber layer defect density (N_t) also influences the device performance, and after a certain value, the performance parameters start to decrease due to the origination of non-radiative recombination. The defects in the absorber layer are inevitable; some common forms are Frenkel defects, Schottky, interstitial and lattice vacancy. These defects may result from self-doping, which introduces deep or shallow band gap energy levels [47]. Eventually, charge carriers are suspected to trap and assist non-radiative electron-hole recombination [48]. For each of the proposed material's based cell, the behavior is shown in Fig. 6(a–d) by varying it in a range of 2.5×10^{11} to 2.5×10^{17} cm^{-3}, with the rest of the other parameters kept intact. The increase in N_t reduces diffusion length compared to the absorber thickness, thus reducing the J_{sc} values due to recombination loss. It can be observed from Fig. 6 that the performance of the cell is higher for smaller N_t values. The highest value of efficiency is obtained for 2.5×10^{11} cm^{-3}, which remains relatively constant up to 2.5×10^{13} cm^{-3} for all ETL materials because the diffusion length is greater here as compared to that of absorber, and does not let N_t to affect J_{sc}, the recombination being low. Similarly, V_{oc}, J_{sc} and FF values remain constant in this region, therefore the optimum value for N_t is set to be 2.5×10^{13} cm^{-3} where the peak efficiencies obtained are 17.90%, 18.87%, 16.33%,
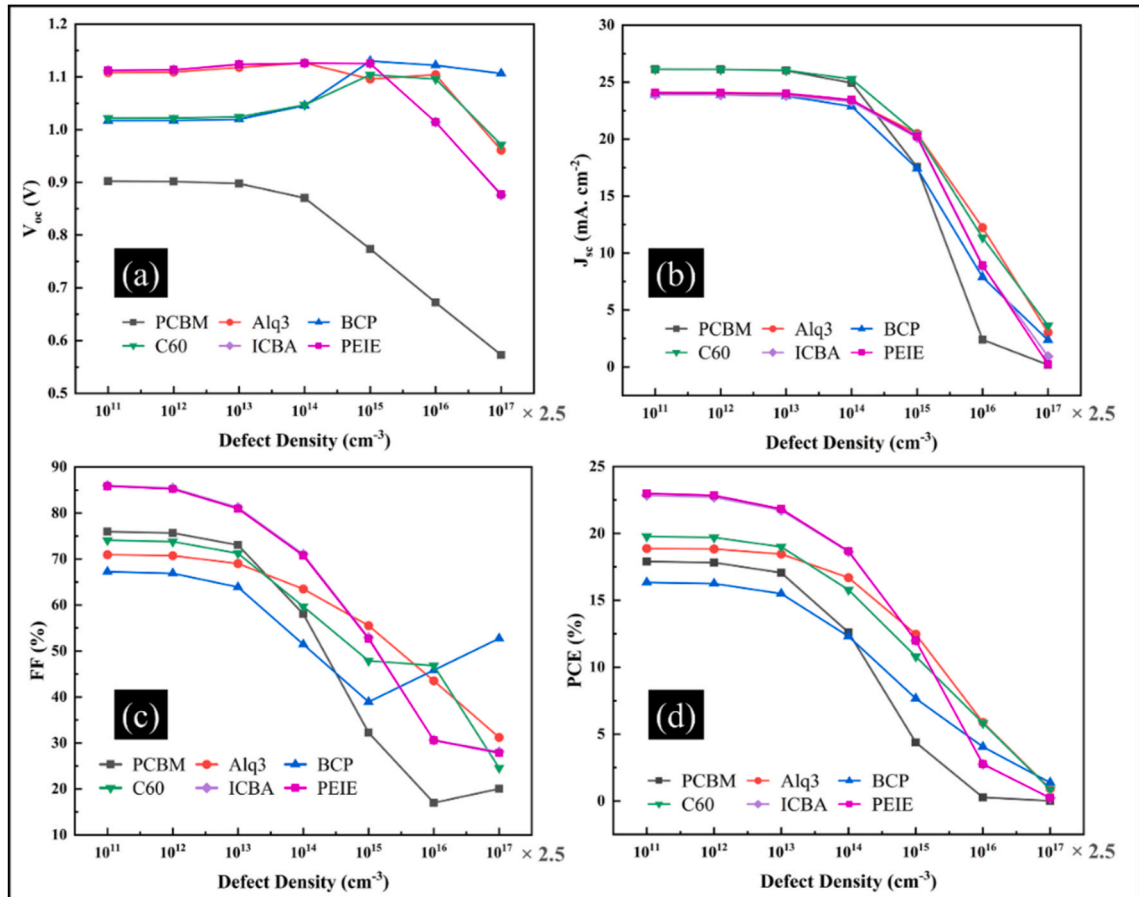
Fig. 6. The effect of change of defect density (N_t) of absorber on (a) V_{oc} (V), (b) J_{sc} (mA/cm^2), (c) FF (%) and (d) PCE (%) by varying it from 2.5×10^{11} to 2.5×10^{17} cm^{-3}.

19.78%, 22.85% and 22.99% for PCBM, Alq$_3$, BCP, C$_{60}$, ICBA and PEIE, respectively. The highest current of 26.12 mA cm^{-2} is achieved for C$_{60}$ and PCBM, whereas the peak voltage of 1.11 V is obtained for PEIE, and the highest FF value is realized for ICBA which is 86.01%.

3.5. Effect of defect-density of interface of perovskite/ETL

In order to passivate recombination defects and ion migration or increase ETL and HTL carrier mobility, interfacial engineering is employed. The interface defects cause high resistance; they generate interface trap levels, increasing recombination and decreasing performance. The device performance is highly influenced by interface defect density when it exceeds a certain level, as shown in Fig. 7 (a–d) when the defect density of IDL is varied from 10^{13} to 10^{21} cm^{-3}. The results indicate that the highest admissible value not affecting the output values is up to 10^{16} cm^{-3}, where higher values indicate a higher rate of recombination of the charge carrier at the interface. Therefore, 1×10^{16} cm^{-3} has been selected for further analyses of each device. The PCE values achieved in this case for PCBM, Alq$_3$, BCP, C$_{60}$, ICBA, and PEIE are 16.98%, 18.45%, 14.40%, 18.97%, 21.70%, and 21.84%, respectively.

3.6. Effect of absorber carrier mobility (μ)

The ion migration and charge carrier mobility (μ) are also vital in determining the performance of the device. 'μ' determines the ease of movement of electrons and holes among layers and towards the corresponding electrodes. An optimum value of μ controls the recombination rate and improves carrier concentration. The current density is proportional to μ; thus, its higher values lead to larger J_{sc} values. The rise in J_{sc} and FF with μ is due to the decrease in device series resistance. To study the impact of charge transport μ is varied both for holes and electrons from 0.01 to 100 cm^2.V^{-1}.s^{-1}. It is shown in Fig. 8(a–d) that the device performance tends to improve only in 0.01–0.1 cm^2.V^{-1}.s^{-1}, where the carrier transportation is improved, and recombination is suppressed. However, beyond 10^0 cm^2.V^{-1}.s^{-1}, the J_{sc} and PCE are not much affected as carrier diffusion increases. The highest values of PCE obtained are
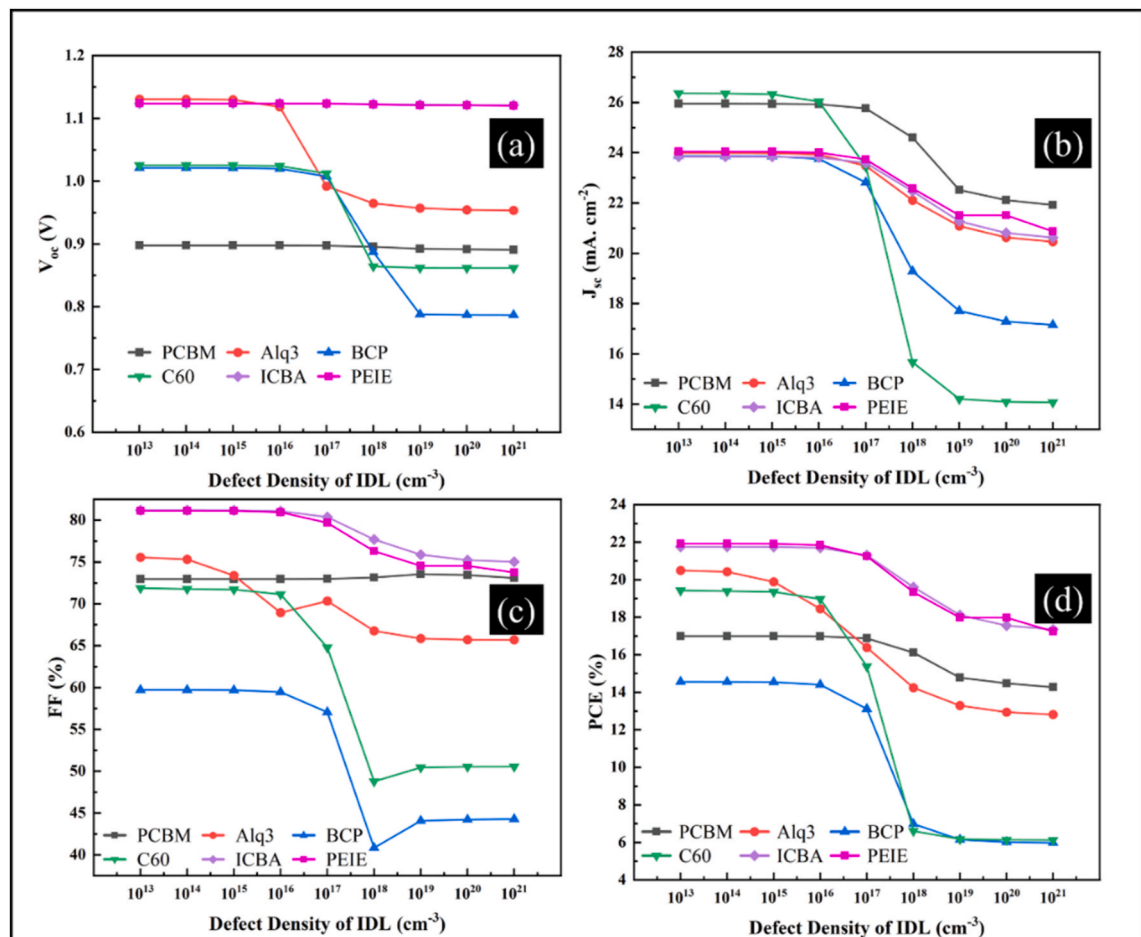
Fig. 7. The effect of variation of absorber/ETL interface defect density by varying it from 10^{13} to 10^{21} cm^{-3} on (a) V$_{oc}$ (V), (b) J$_{sc}$ (mA/cm^2), (c) FF (%) and (d) PCE (%).
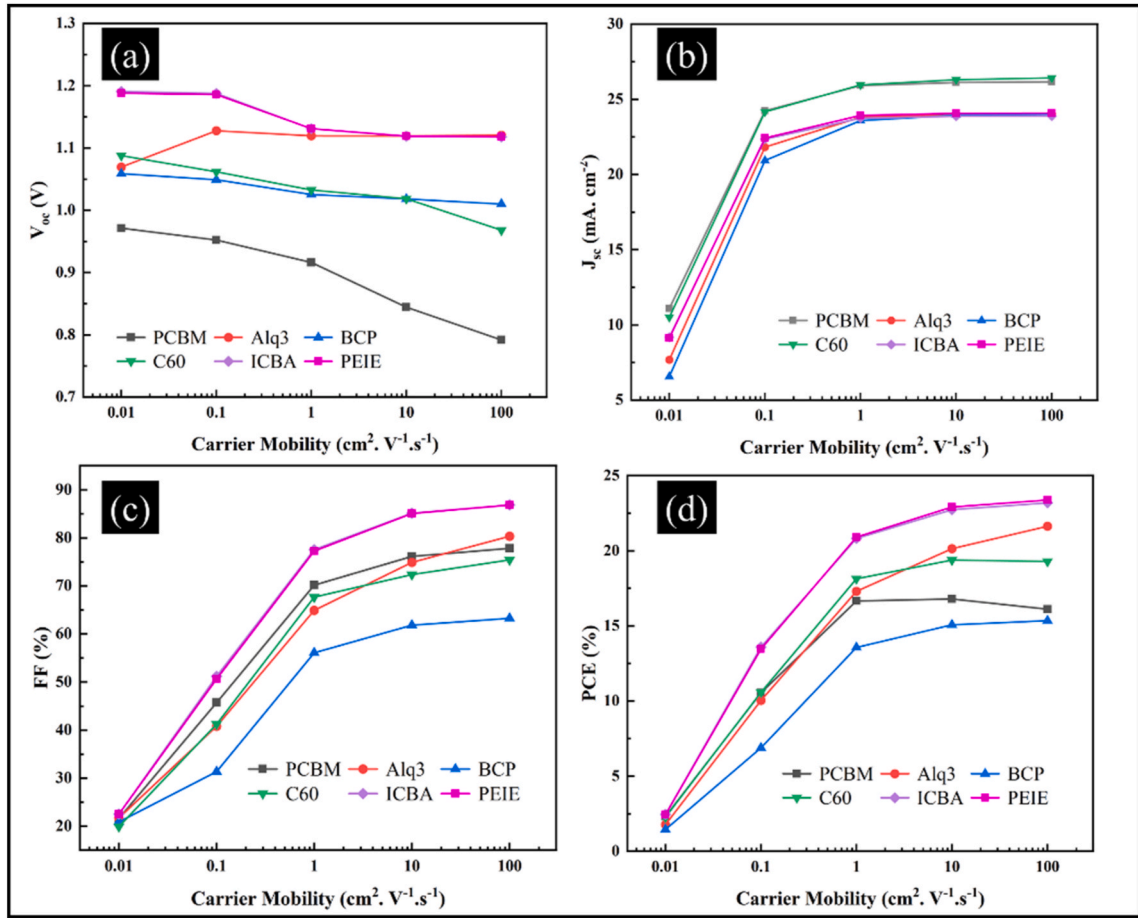
Fig. 8. Effect on performance parameters of device (a) V_{oc} (V), (b) J_{sc} (mA.cm^{-2}), (c) FF (%) and (d) PCE (%) when carrier mobility (μ) varies from 10^{-2} to 10^1 cm^2.V^{-1}.s^{-1} for different ETL materials.

16.79%, 21.63%, 15.34%, 19.38%, 23.18%, and 23.37% for PCBM, Alq$_3$, BCP, C$_{60}$, ICBA, and PEIE, respectively.

3.7. Effect of carrier diffusion length and lifetime of carriers

Another design parameter for a solar cell device is the diffusion length which is the average length that a carrier travels from the point of generation until its recombination. Diffusion length shortens when a material is highly doped because of higher recombination rates. On the other hand, higher diffusion lengths for a given material indicate that the material has longer lifetimes. Both diffusion length and minority carrier lifetime depend highly on the magnitude and type of recombination in a semiconductor. The diffusion length relates to a parameter known as the diffusion coefficient with a square root relation directly related to carrier mobility [49] (Equation (1)). The increase in diffusion length increases J_{sc} due to reduced recombination [50]. Thus, larger mobility values lead to larger diffusion lengths and support higher efficiency values.

$$L_D = \sqrt{D_\tau} \qquad (1)$$

The semiconductor wafer fabrication method and the processing majorly affect the diffusion length. In addition, defect density and diffusion length too are interlinked. The effect of variation of diffusion length on performance parameters is studied in the range of 0.3–1 μm, where the device parameters are listed in Table 3 and shown in Fig. 9(a–d).

3.8. Effect of series and shunt resistance

For a better-performing solar cell design, the series resistance (R_s) should be low, and shunt resistance (R_{sh}) should be high. R_s directly impacts FF and J_{sc}, whereas R_{sh} affects the photo-voltage and photo-generated current. These resistances of the device also limit the performance in the form of several losses, such as leakage current and trapping of charge carriers at interfaces [51]. The typical J-V behavior of a cell is described using Shockley Equations (2) and (3), respectively [52].

Table 3

The performance parameters of the device with different ETLs under variation of Carrier diffusion length (μm) from 0.3 to 1 and corresponding carrier lifetime (ns) from 17 to 190 ns. The quantities V_{oc}, J_{sc}, FF, and PCE are measured in V, mAcm^{-2}, %, and %, respectively.

ETL Material	Paramateer	Diffusion Lenght (μm)								ETL Material	Paramateer	Diffusion Lenght (μm)							
		0.3	0.4	0.5	0.6	0.7	0.8	0.9	1.0			0.3	0.4	0.5	0.6	0.7	0.8	0.9	1.0
		Carrier Lifetime (ns)										Carrier Lifetime (ns)							
		17	31	48	70	96	120	160	190			17	31	48	70	96	120	160	190
PCBM	V_{oc}	0.867	0.879	0.886	0.891	0.893	0.895	0.896	0.897	**C$_{60}$**	V_{oc}	1.05	1.04	1.03	1.03	1.02	1.02	1.02	1.02
	J_{sc}	24.85	25.39	25.65	25.80	25.88	25.94	25.98	26.01		J_{sc}	25.27	25.65	25.83	25.94	26.01	26.04	26.07	26.09
	FF	56.67	62.24	65.95	68.52	70.25	71.39	72.25	72.94		FF	58.62	62.51	65.23	67.18	68.59	69.53	70.26	70.80
	PCE	12.21	13.90	14.99	15.74	16.25	16.58	16.83	17.02		PCE	15.57	16.67	17.43	17.96	18.35	18.60	18.80	18.95
Alq$_3$	V_{oc}	1.125	1.12	1.13	1.12	1.12	1.12	1.12	1.11	**ICBA**	V_{oc}	1.13	1.12	1.13	1.13	1.13	1.12	1.12	1.12
	J_{sc}	23.30	23.56	23.70	23.79	23.85	23.88	23.91	23.93		J_{sc}	23.26	23.50	23.63	23.70	23.75	23.78	23.80	23.82
	FF	63.07	64.74	65.80	66.80	67.50	68.10	68.59	68.96		FF	70.23	73.85	75.44	77.24	78.64	79.63	80.63	81.34
	PCE	16.54	17.20	17.62	17.91	18.12	18.26	18.37	18.45		PCE	18.62	19.59	20.26	20.75	21.11	21.37	21.60	21.77
BCP	V_{oc}	1.04	1.03	1.02	1.02	1.02	1.02	1.02	1.01	**PEIE**	V_{oc}	1.139	1.12	1.13	1.13	1.13	1.12	1.12	1.12
	J_{sc}	22.78	23.24	23.46	23.59	23.67	23.72	23.76	23.78		J_{sc}	23.45	23.69	23.82	23.90	23.94	23.97	24.01	24.01
	FF	50.74	54.78	57.68	59.80	61.36	62.42	63.27	63.90		FF	70.12	73.72	75.30	77.11	78.38	79.49	80.48	81.20
	PCE	12.11	13.18	13.92	14.46	14.85	15.12	15.33	15.49		PCE	18.74	19.72	20.39	20.89	21.25	21.51	21.74	21.91
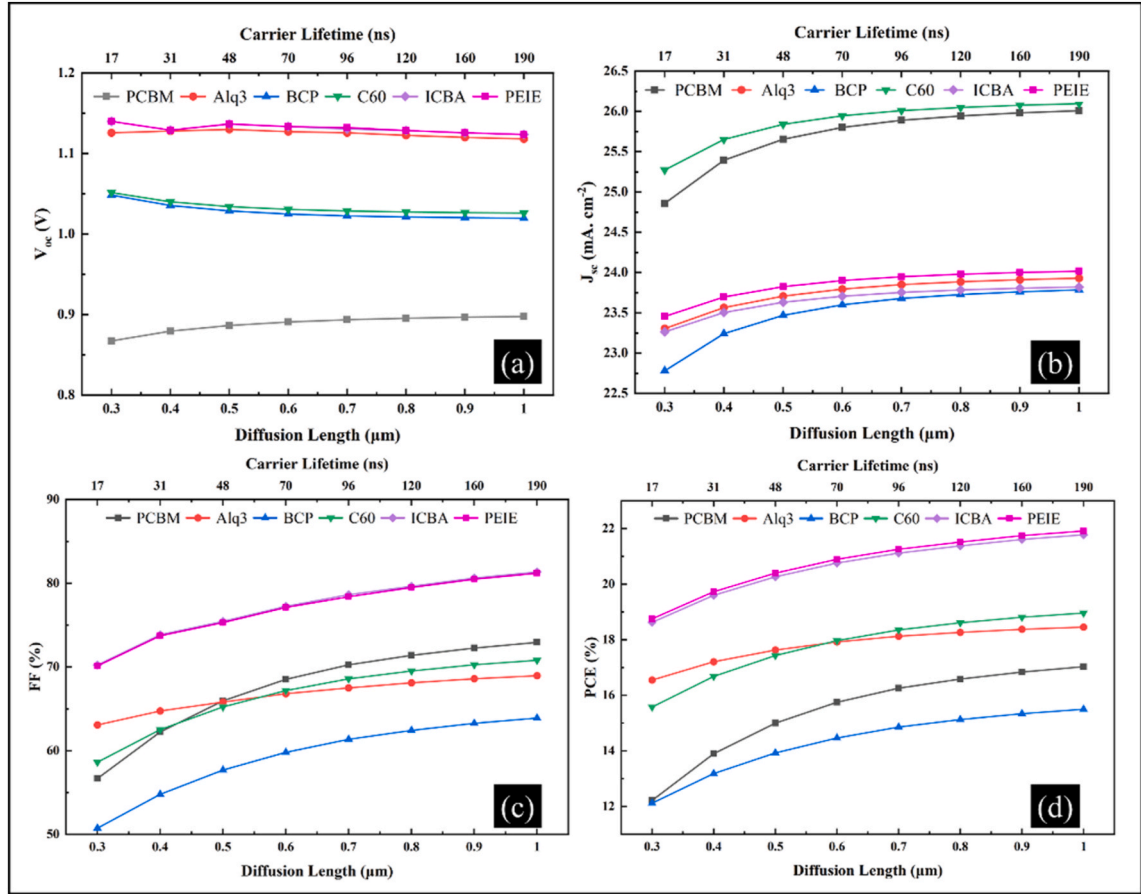
Fig. 9. The change of diffusion length is reflected in a change in carrier lifetime, the effect on (a) V_{oc} (V), (b) J_{sc} (mA.cm^{-2}), (c) FF (%), and (d) PCE (%) of L_p, L_n from 0.3 μm to 1 μm with τ_p and τ_n from 17 to 190 ns.

$$V_{oc} = \left(\frac{nkT}{q}\right)\ln\left[\frac{J_{ph}}{J_0}\left(1 - \frac{V_{oc}}{J_{ph}R_{sh}}\right)\right] \tag{2}$$

$$J_{sc} = J_{ph} - J_0\left[e^{\frac{q(V-JR_s)}{nkT}} - 1\right] - \frac{V - JR_s}{R_{sh}} \tag{3}$$

$$FF = \frac{P_{max}}{V_{oc}J_{sc}} \tag{4}$$

$$PCE = \frac{J_{sc} \times V_{oc} \times FF}{P_{in}} \tag{5}$$

J_{ph} is photocurrent density, J_0 is reverse bias saturation current density, n represents the diode ideality factor, k is the Boltzmann constant, and T is the operating temperature.

In an ideal scenario, R_s is zero, while R_{sh} is infinite. Here, we have varied R_s from 0, i.e., ideal to 100 Ω cm^{-2}, and observed from Fig. 10 (a) that V_{oc} remains constant, which is in alignment with Equation (2). However, it is seen from Fig. 10 (b) that the value of J_{sc} decreases as the value of R_s increases, which again is in agreement with Shockley's equation. Similarly, the values of FF given in Equation (4) decrease with an increase in R_s (Fig. 10 (c)) as the maximum obtained power in the absence and presence of R_s are different [53]. In the same way, PCE given by Equation (5) also decreases with an increase in R_s values with the highest PCE for zero series resistance (Fig. 10 (d)). On the other hand, it can be seen from Fig. 11(a–d) that the device performance is not much affected by variation in R_{sh} from 10^4 Ω cm^{-2} to 10^8 Ω cm^{-2}.

3.9. Effect of variation of operating temperature

Any perovskite composition is susceptible to temperature as they contain organic cations, and temperature analysis on the aging
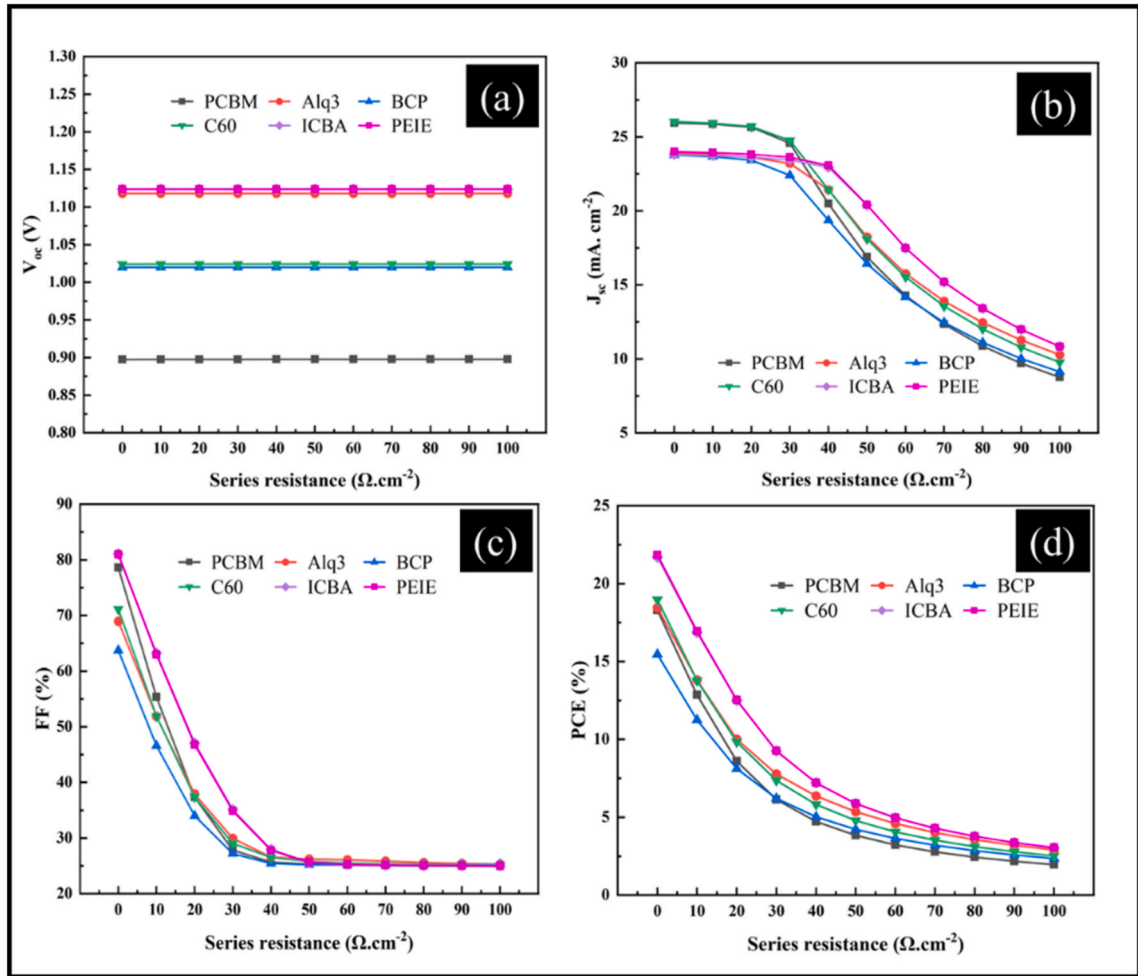
Fig. 10. Effect of variation of series resistance from 0 to 100 $\Omega.cm^{-2}$ on (a) Voc (V), (b) J_{sc} (mAcm^{-2}), (c) FF (%), and (d) PCE (%).

effect for outdoor operations is crucial. The device's behavior is analyzed under the operating temperature variation from 25 to 60 °C. It is evident from Fig. 12(a–d) that the values of V_{oc}, FF, and PCE decrease due to increased series resistance and interfacial defects formation, which lead to reduced diffusion length.

3.10. Effect of back metal contact work function

In a conventional design of a PSC, there is a noble metal back contact [54]. The study is carried out in the light of the variation of work function (Φ) of the back metal to see the ohmic effect at metal contact in the range 4.50–6.0 eV, which correspond to the Φ values for Au, Ag, Fe, Cu, and Pt [55]. The performance parameters are shown in Fig. 13(a–d), and it is seen that J_{sc} is relatively constant; V_{oc} and PCE keep increasing with Φ values until it reaches 5.50 eV, and that of FF has only a slower increase. At the metal-semiconductor interface, band bending takes place, reducing the barrier size of the majority carriers. At the lower values of Φ, a Schottky junction is formed; thus, a high-valued Φ is needed for ohmic contact, and it can be seen from Fig. 13(a–d) that the application of carbon back contact with an Φ value of 5.0 eV leads to significantly high performance. The carbon contact is encouraged due to its cost-effectiveness in comparison to metals.

3.11. Quantum efficiency

Fig. 14 shows the quantum efficiency (QE) over a wavelength range of 300–900 nm for proposed HTL-free structure for each ETL material. The results show that the light absorption of all the materials is almost alike throughout the visible region. The efficient light absorption leads to an improved QE response, resulting in higher J_{sc} values.
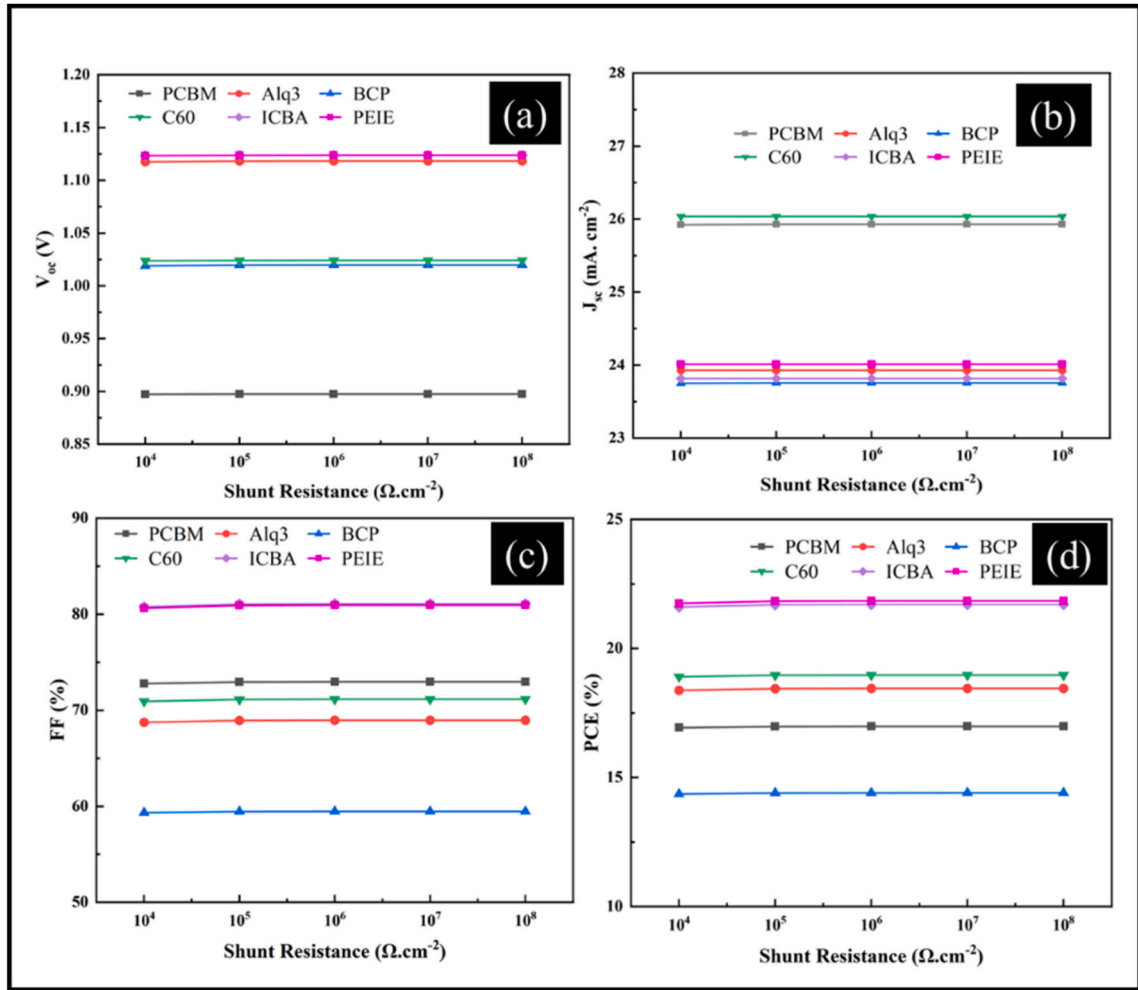
Fig. 11. Effect of variation of shunt resistance from 10^4 Ω cm^{-2} to 10^8 Ω cm^{-2} on (a) Voc (V), (b) J_{sc} (mA.cm^{-2}), (c) FF (%), and (d) PCE (%).

3.12. Device stability improvement

One of the major design concerns for a PSC is its instability. Significant work has so far been done to improve the device's stability against exposure to moisture, oxygen, heat, and UV radiation, which hinders the commercialization of these devices [56]. Interface engineering has been a continuously driven area of research [57,58] for controlling interface losses and electron/hole recombination in addition to being in favor of moisture control [59], thereby increasing the stability and performance of the devices. In this connection, ETLs, in combination with an interlayer of materials, have been studied where the inserted layer reduces electrical losses by avoiding undesirable shunt paths while promoting electron transfer while not affecting absorber performance. The additional purpose of the layer is to protect the device against degradation as the organic material stability is lower. Bismuth triiodide (BiI$_3$) is a non-toxic, earth-abundant, high-performance absorber that is a good candidate for photovoltaic absorption in MAPbI$_3$-based solar cells [27]. It has shown potential for charge transport properties, defect tolerance, and recombination lifetime, having a bandgap of ~1.8 eV. As another alternative, ZnO has attracted attention as interlayer material with high electron mobility, environmental stability, and optical transparency [60]. Kwon et al. have presented an efficient and planar perovskite MAPbI$_3$ solar cell with PCE of 16.39% by introducing PCBM/ZnO NPs interlayers [28] with a HTL device, which we have achieved to be 16.86% in HTL free device. LiF has been used as a buffer layer and has been found to increase the PCE of the presented device [30] from 16.01% to 18.18% by improving its electrical performance. Here, we have introduced layers of BiI$_3$, ZnO and LiF on ETL materials as shown in Fig. 15 (a), whose material properties are taken from Refs. [36,61,62]. All of them are found to have optimum performance for 10 nm thickness. The cell efficiencies are only very nominally compromised for some cases and have improved in many other cases with their values given in Fig. 15 (b–g). The improvement is an indication of better exciton dissociation and suited electron transfer because of energy level alignment between perovskite and ETL with interlayer. The basic purpose of these layers is to enhance stability against environment and heat [63]. A comparison of the proposed simulated device performance is given in Table 4 for the organic ETL materials we particularly have employed in this work.
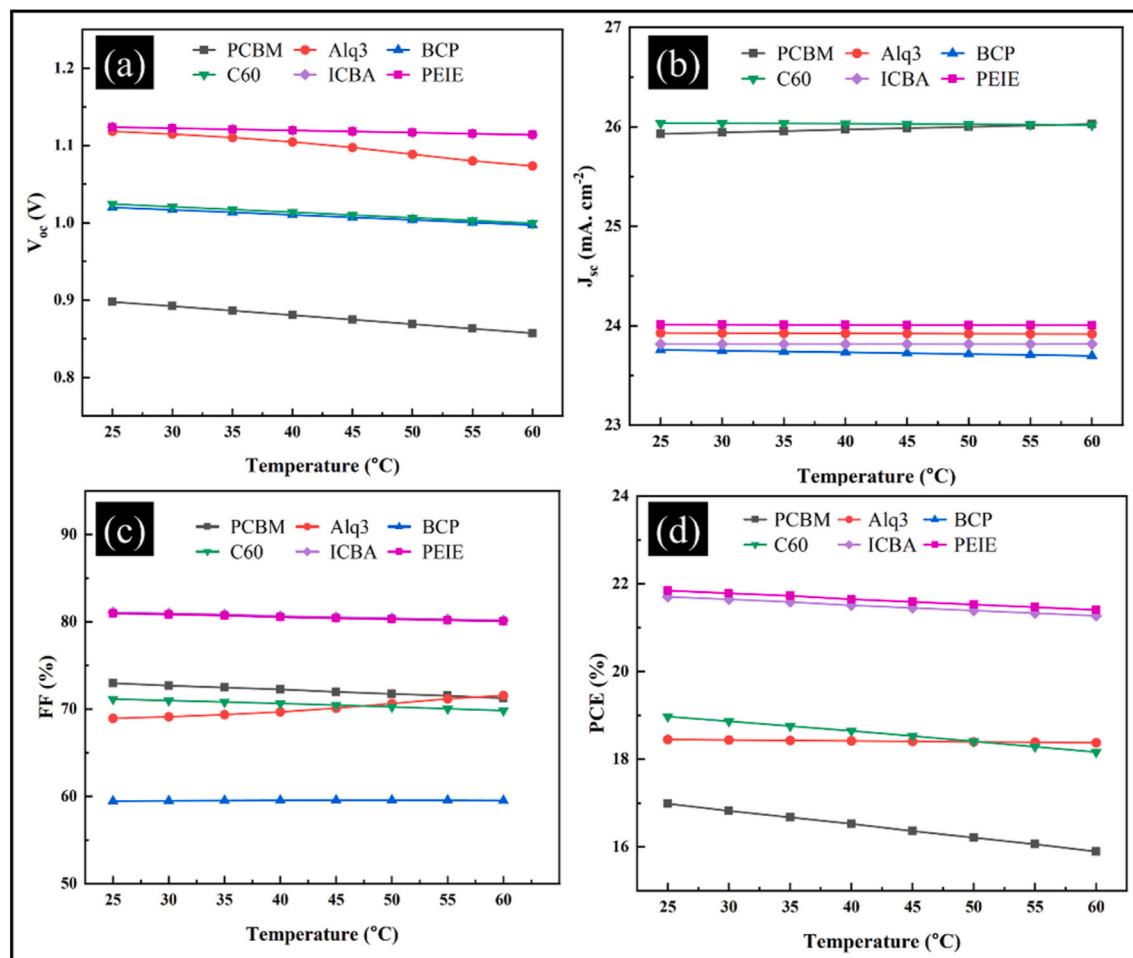
Fig. 12. Effect of variation of operating temperature on the device from 25 to 60 °C on (a) V_{oc} (V), (b) J_{sc} (mA/cm^2), (c) FF (%), and (d) PCE (%).

4. Conclusion

An HTL-free CH$_3$NH$_3$PbI$_3$ PSC is investigated using organic ETL materials such as PCBM, Alq$_3$, BCP, C$_{60}$, ICBA, and PEIE. The device assumes FTO/ETL/IDL/CH$_3$NH$_3$PbI$_3$/C structure, which was numerically optimized using SCAPS-1D software. The effect of various factors such as absorber layer thickness, acceptor density, the defect density of absorber as well as IDL, carrier mobility, diffusion length, lifetime of charge carriers, donor concentration of ETL, series and shunt resistances, work function of back metal contact and operating temperature was examined in detail. The optimum thickness for each device is different such as 1000 nm for Alq$_3$, 1200 nm for BCP, 1100 nm for C$_{60}$, 1000 nm for PCBM, and 2000 for ICBA and PEIE-based devices, respectively. The value of N$_t$ is optimized to be 2.5×10^{13} cm^{-3} as its excessive value can cause higher recombination of charge carriers, thus reducing the performance. N$_A$ is chosen to be 10^{17} cm^{-3} for each case, with the defect level of IDL to be 10^{16} cm^{-3}. The back metal contact is made of carbon due to its being cost-friendly. It has been established that carbon-based HTL-free PSC is viable for realizing high performance, easy to manufacture, and a low-cost solar cell. The highest achieved PCE for PCBM, Alq$_3$, BCP, C$_{60}$, ICBA, and PEID-based devices are 22.85%, 19.08%, 20.99%, 25.51%, 23.91%, and 22.53%, respectively. The C$_{60}$-based cell has been found to outperform with V_{oc} of 1.29 V, J_{sc} of 23.76 mA/cm^2, and FF of 82.67%. Since ETLs being organic lack stability, an interlayer of BiI$_3$, LiF, and ZnO is employed to ensure the device stability, thereby not compromising the device performance. We believe that the results predicted by our simulation study can be obtained experimentally if the losses experienced during fabrication processes are mitigated.

Data availability statement

Data will be available upon reasonable request.
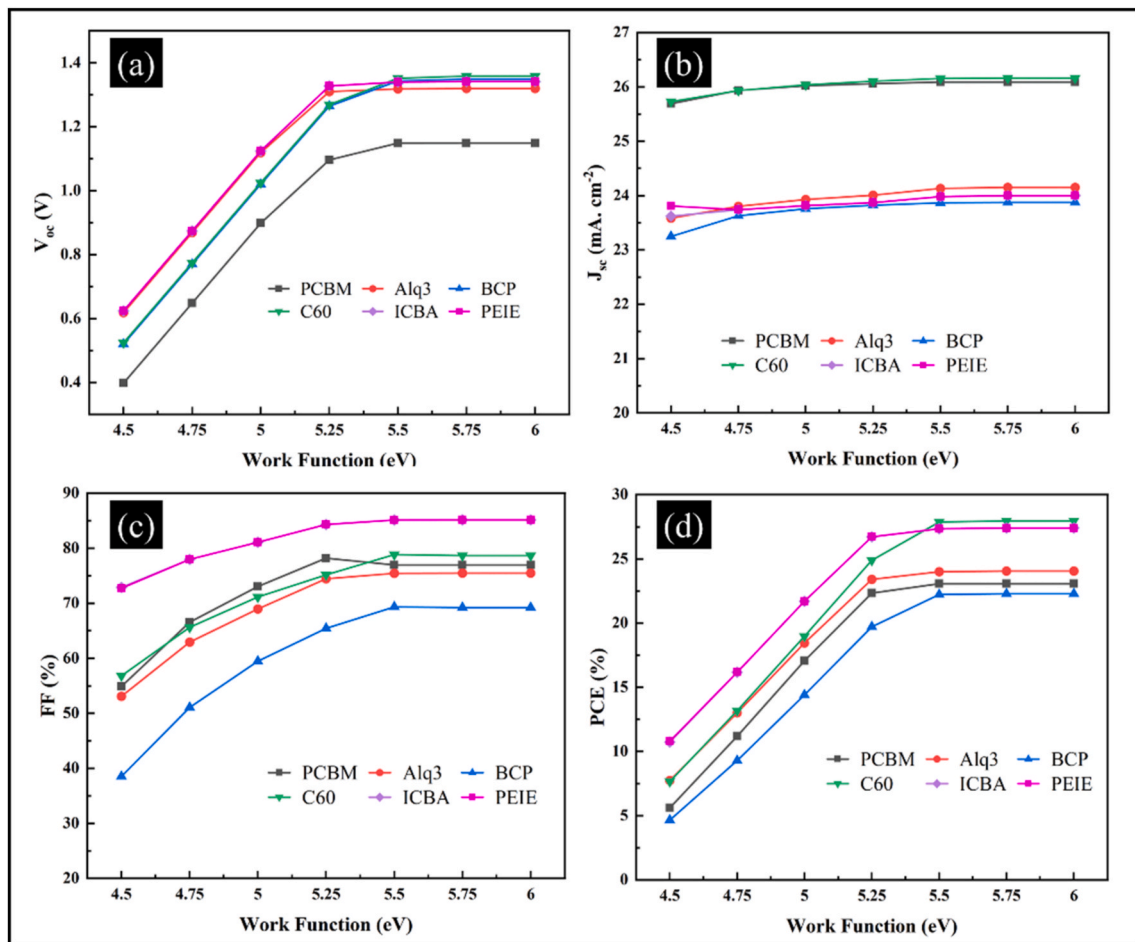
Fig. 13. The effect of variation of back metal work function on (a) Voc (V), (b) Jsc (mA.cm^{-2}), (c) FF (%), and (d) PCE (%) in the range 4.50–6.0 eV.
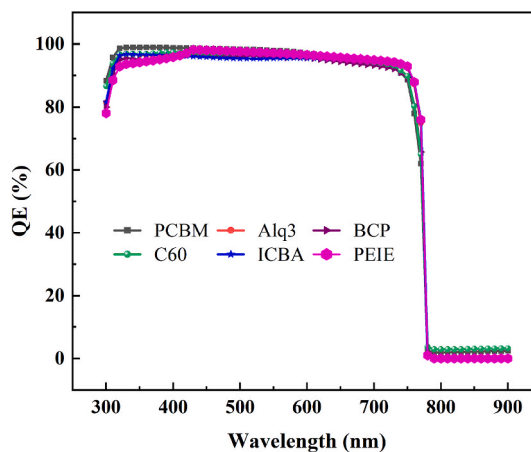
Fig. 14. The quantum efficiency of the proposed cell in the broadband visible range of wavelength (300–900 nm).

CRediT authorship contribution statement

Sumbel Ijaz: Writing – original draft, Visualization, Software, Resources, Methodology, Data curation, Conceptualization. **Ehsan Raza:** Writing – review & editing, Visualization, Resources, Formal analysis, Data curation. **Zubair Ahmad:** Writing – review &
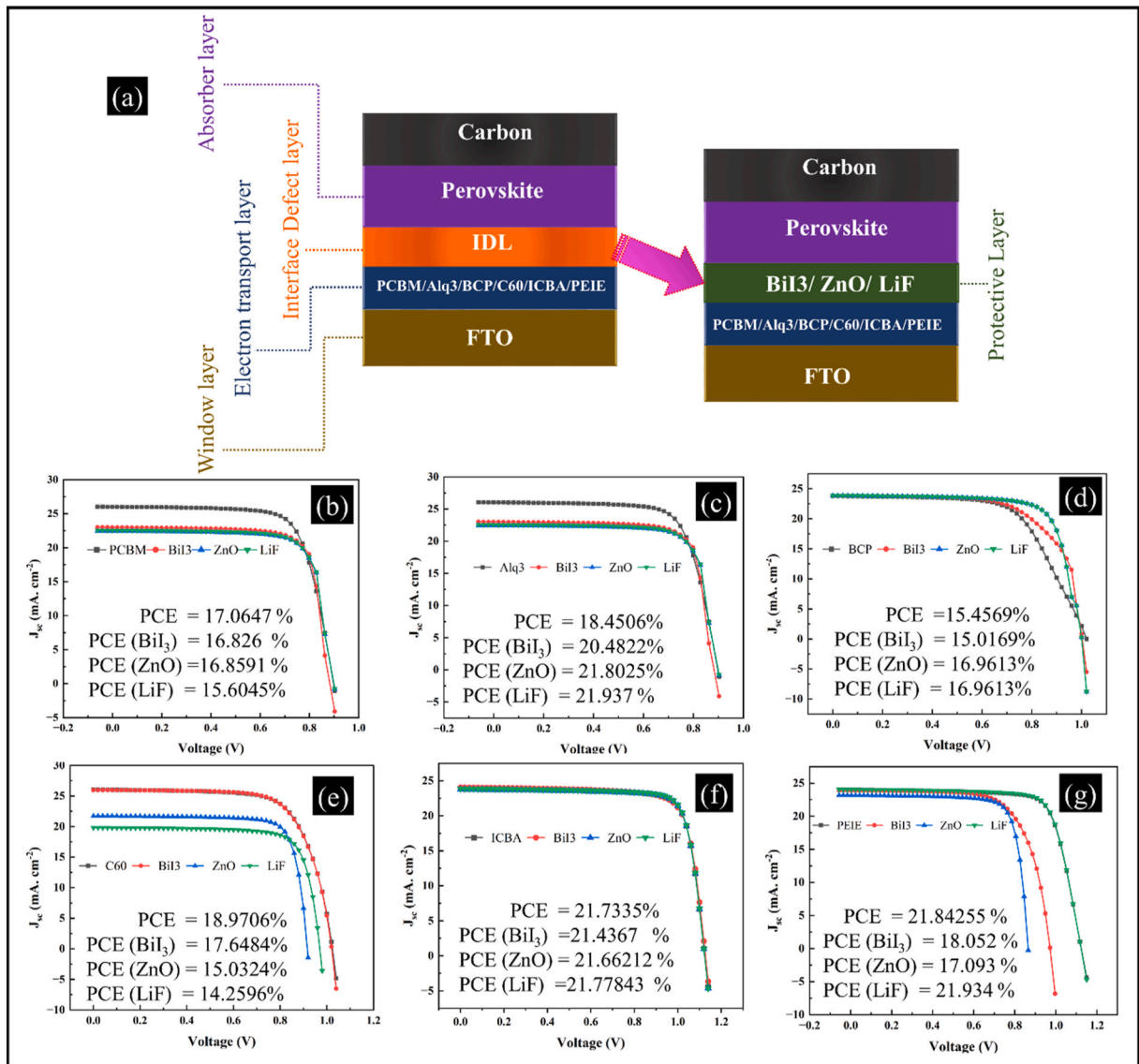
Fig. 15. JV characteristics of the devices after introducing interlayers (BiI₃, ZnO, and LiF) between the perovskite and ETL layer. (a) the change in structure, the (b) PCBM-, (c) Alq₃- (d) BCP- (e) C₆₀- (f) ICBA- and (g) PEIE-based devices. Each figure inset shows the PCE values in different configurations.

Table 4
The comparison of the device performance with already presented devices.

ETL material	PCE	Ref.
PCBM/F8BT	19.28%	[64]
PCBM/Triton X-100	15.68%	[65]
TiO₂-c/Alq₃	12.48%	[66]
PCBM:BCP	13.11%	[67]
C₆₀	19.10%	[68]
C₆₀	17.15%	[69]
ICBA-tran3	18.5%	[70]
ICBA:PCBM	18.14%	[71]
ZnO:PEIE	8.03%	[72]
C₆₀	25.51%	The presented work.

editing, Validation, Supervision, Formal analysis, Conceptualization. **Haris Mehmood:** Writing – review & editing. **Muhammad Zubair:** Writing – review & editing. **Muhammad Qasim Mehmood:** Writing – review & editing, Validation, Supervision. **Yehia Massoud:** Writing – review & editing, Funding acquisition.

Declaration of competing interest

The authors declare that they have no known competing financial interests or personal relationships that could have appeared to influence the work reported in this paper.

Acknowledgements

References

[1] J. Zhoa, A. Wang, M. Taouk, F. Yun, A. Ebong, A.W. Stephens, S.R. Wenham, M.A. Green, 20% efficient silicon solar cell modules, Conf. Rec. IEEE Photovolt. Spec. Conf. (1993) 1246–1249, https://doi.org/10.1109/pvsc.1993.346943.

[2] L. Schmidt-Mende, V. Dyakonov, S. Olthof, F. Ünlü, K.M.T. Lê, S. Mathur, A.D. Karabanov, D.C. Lupascu, L.M. Herz, A. Hinderhofer, F. Schreiber, A. Chernikov, D.A. Egger, O. Shargaieva, C. Cocchi, E. Unger, M. Saliba, M.M. Byranvand, M. Kroll, F. Nehm, K. Leo, A. Redinger, J. Höcker, T. Kirchartz, J. Warby, E. Gutierrez-Partida, D. Neher, M. Stolterfoht, U. Würfel, M. Unmüssig, J. Herterich, C. Baretzky, J. Mohanraj, M. Thelakkat, C. Maheu, W. Jaegermann, T. Mayer, J. Rieger, T. Fauster, D. Niesner, F. Yang, S. Albrecht, T. Riedl, A. Fakharuddin, M. Vasilopoulou, Y. Vaynzof, D. Moia, J. Maier, M. Franckevičius, V. Gulbinas, R.A. Kerner, L. Zhao, B.P. Rand, N. Glück, T. Bein, F. Matteocci, L.A. Castriotta, A. Di Carlo, M. Scheffler, C. Draxl, Roadmap on organic-inorganic hybrid perovskite semiconductors and devices, Apl. Mater. 9 (2021), https://doi.org/10.1063/5.0047616.

[3] M.K. Hossain, G.F.I. Toki, A. Kuddus, M.K.A. Mohammed, R. Pandey, J. Madan, S. Bhattarai, M.F. Rahman, D.K. Dwivedi, M. Amami, H. Bencherif, D. P. Samajdar, Optimization of the architecture of lead-free CsSnCl3-perovskite solar cells for enhancement of efficiency: a combination of SCAPS-1D and wxAMPS study, Mater. Chem. Phys. 308 (2023), https://doi.org/10.1016/j.matchemphys.2023.128281.

[4] M.A. Green, A. Ho-Baillie, H.J. Snaith, The emergence of perovskite solar cells, Nat. Photonics 8 (2014) 506–514, https://doi.org/10.1038/nphoton.2014.134.

[5] H.S. Kim, C.R. Lee, J.H. Im, K.B. Lee, T. Moehl, A. Marchioro, S.J. Moon, R. Humphry-Baker, J.H. Yum, J.E. Moser, M. Grätzel, N.G. Park, Lead iodide perovskite sensitized all-solid-state submicron thin film mesoscopic solar cell with efficiency exceeding 9, Sci. Rep. 2 (2012), https://doi.org/10.1038/srep00591.

[6] J. Park, J. Kim, H.-S. Yun, M.J. Paik, E. Noh, H.J. Mun, M.G. Kim, T.J. Shin, S. Il Seok, Controlled growth of perovskite layers with volatile alkylammonium chlorides, Nature (2023), https://doi.org/10.1038/s41586-023-05825-y.

[7] Y.H. Khattak, F. Baig, A. Shuja, L. Atourki, K. Riaz, B.M. Soucase, Device optimization of PIN structured perovskite solar cells: impact of design variants, ACS Appl. Electron. Mater. 3 (2021) 3509–3520, https://doi.org/10.1021/acsaelm.1c00460.

[8] M.K. Hossain, S. Bhattarai, A.A. Arnab, M.K.A. Mohammed, R. Pandey, M.H. Ali, M.F. Rahman, M.R. Islam, D.P. Samajdar, J. Madan, H. Bencherif, D. K. Dwivedi, M. Amami, Harnessing the potential of CsPbBr3-based perovskite solar cells using efficient charge transport materials and global optimization, RSC Adv. 13 (2023) 21044–21062, https://doi.org/10.1039/D3RA02485G.

[9] S.D. Stranks, S.D. Stranks, G.E. Eperon, G.E. Eperon, G. Grancini, G. Grancini, C. Menelaou, C. Menelaou, M.J.P. Alcocer, M.J.P. Alcocer, T. Leijtens, T. Leijtens, L.M. Herz, L.M. Herz, A. Petrozza, A. Petrozza, H.J. Snaith, H.J. Snaith, Electron-hole diffusion lengths exceeding 1 micrometer in an organometal trihalide perovskite absorber, Science 342 (2013) 341–344. http://www.sciencemag.org/cgi/doi/10.1126/science.1243982%0Apapers3://publication/doi/10.1126/science.1243982.

[10] M.M. Lee, J. Teuscher, T. Miyasaka, T.N. Murakami, H.J. Snaith, Efficient hybrid solar cells based on meso-superstructured organometal halide perovskites, Science. 338 (2012) 643–647, https://doi.org/10.1126/science.1228604.

[11] A. Mei, X. Li, L. Liu, Z. Ku, T. Liu, Y. Rong, M. Xu, M. Hu, J. Chen, Y. Yang, M. Grätzel, H. Han, A hole-conductor-free, fully printable mesoscopic perovskite solar cell with high stability, Science 345 (2014) 295–298, https://doi.org/10.1126/science.1254763.

[12] L. Huang, Z. Hu, J. Xu, X. Sun, Y. Du, J. Ni, H. Cai, J. Li, J. Zhang, Efficient planar perovskite solar cells without a high temperature processed titanium dioxide electron transport layer, Sol. Energy Mater. Sol. Cells 149 (2016) 1–8, https://doi.org/10.1016/j.solmat.2015.12.033.

[13] G.X.N. Mathews, S. Sun, S.S. Lim, Y.M. Lam, M. Grätzel, S. Mhaisalkar, T.C. Sum, Long-range balanced electron- and hole-transport lengths in organic-inorganic CH3NH3PbI3, Science 342 (2013) 344–346.

[14] L. Zhang, T. Liu, L. Liu, M. Hu, Y. Yang, A. Mei, H. Han, The effect of carbon counter electrodes on fully printable mesoscopic perovskite solar cells, J. Mater. Chem. A. 3 (2015) 9165–9170, https://doi.org/10.1039/c5ta04647a.

[15] K. Ke, K.K. Kondamareddy, F. Gao, X. Zhang, X. Yuan, Fabrication of highly efficient and stable hole-transport material-free perovskite solar cells through morphology and interface engineering: full ambient process, Energy Technol. 7 (2019), https://doi.org/10.1002/ente.201900446.

[16] Z. Ku, Y. Rong, M. Xu, T. Liu, H. Han, Full printable processed mesoscopic CH3NH3PbI3/TiO2 heterojunction solar cells with carbon counter electrode, Sci. Rep. 3 (2013) 3132, https://doi.org/10.1038/srep03132.

[17] L. Bokobza, J.-L. Bruneel, M. Couzi, Raman Spectra of Carbon-Based Materials (from Graphite to Carbon Black) and of Some Silicone Composites, C 1 (2015), https://doi.org/10.3390/c1010077.

[18] S. Zouhair, S.-M. Yoo, D. Bogachuk, J.P. Herterich, J. Lim, H. Kanda, B. Son, H.J. Yun, U. Würfel, A. Chahboun, M.K. Nazeeruddin, A. Hinsch, L. Wagner, H. Kim, Employing 2D-perovskite as an electron blocking layer in highly efficient (18.5%) perovskite solar cells with printable low temperature carbon electrode, Adv. Energy Mater. 12 (2022) 2200837, https://doi.org/10.1002/aenm.202200837.

[19] E. Raza, Z. Ahmad, M. Asif, F. Aziz, K. Riaz, M.Q. Mehmood, J. Bhadra, N.J. Al-Thani, Numerical modeling and performance optimization of carbon-based hole transport layer free perovskite solar cells, Opt. Mater. 125 (2022) 112075, https://doi.org/10.1016/j.optmat.2022.112075.

[20] L. Lin, P. Li, Z. Kang, H. Xiong, Y. Chen, Q. Yan, L. Jiang, Y. Qiu, Device design of doping-controlled homojunction perovskite solar cells omitting HTL and exceeding 25% efficiency, Adv. Theory Simulations. 4 (2021), https://doi.org/10.1002/adts.202000222.

[21] W. Shockley, H. Queisser, Detailed balance limit of efficiency of p–n junction solar cells, Renew. Energy (2020) 35–54, https://doi.org/10.4324/9781315793245-44.

[22] W.E.I. Sha, X. Ren, L. Chen, W.C.H. Choy, The efficiency limit of CH3NH3PbI3 perovskite solar cells, Appl. Phys. Lett. 106 (2015), https://doi.org/10.1063/1.4922150.

[23] H. Wei, J. Xiao, Y. Yang, S. Lv, J. Shi, X. Xu, J. Dong, Y. Luo, D. Li, Q. Meng, Free-standing flexible carbon electrode for highly efficient hole-conductor-free perovskite solar cells, Carbon N. Y. 93 (2015) 861–868, https://doi.org/10.1016/j.carbon.2015.05.042.

[24] S. Wu, Z. Li, M.Q. Li, Y. Diao, F. Lin, T. Liu, J. Zhang, P. Tieu, W. Gao, F. Qi, X. Pan, Z. Xu, Z. Zhu, A.K.Y. Jen, 2D metal–organic framework for stable perovskite solar cells with minimized lead leakage, Nat. Nanotechnol. 15 (2020) 934–940, https://doi.org/10.1038/s41565-020-0765-7.

[25] M. Burgelman, P. Nollet, S. Degrave, Modelling polycrystalline semiconductor solar cells, Thin Solid Films 361 (2000) 527–532, https://doi.org/10.1016/S0040-6090(99)00825-1.

[26] M.K. Hossain, A.A. Arnab, D.P. Samajdar, M.H.K. Rubel, M.M. Hossain, M.R. Islam, R.C. Das, H. Bencherif, M.F. Rahman, J. Madan, R. Pandey, S. Bhattarai, M. Amami, D.K. Dwivedi, Design insights into La2NiMnO6-based perovskite solar cells employing different charge transport layers: DFT and SCAPS-1D frameworks, Energy Fuel. 37 (2023) 13377–13396, https://doi.org/10.1016/acs.energyfuels.3c02361.

[27] R.E. Brandt, R.C. Kurchin, R.L.Z. Hoye, J.R. Poindexter, M.W.B. Wilson, S. Sulekar, F. Lenahan, P.X.T. Yen, V. Stevanović, J.C. Nino, M.G. Bawendi, T. Buonassisi, Investigation of bismuth triiodide (BiI3) for photovoltaic applications, J. Phys. Chem. Lett. 6 (2015) 4297–4302, https://doi.org/10.1021/acs.jpclett.5b02022.

[28] S.N. Kwon, J.H. Yu, S.I. Na, A systematic approach to ZnO nanoparticle-assisted electron transport bilayer for high efficiency and stable perovskite solar cells, J. Alloys Compd. 801 (2019) 277–284, https://doi.org/10.1016/j.jallcom.2019.06.089.

[29] X. Liu, H. Yu, L. Yan, Q. Dong, Q. Wan, Y. Zhou, B. Song, Y. Li, Triple cathode buffer layers composed of PCBM, C60, and LiF for high-performance planar perovskite solar cells, ACS Appl. Mater. Interfaces 7 (2015) 6230–6237, https://doi.org/10.1021/acsami.5b00468.

[30] L. Chen, C. Xu, W. Hu, Y. Yao, L. Niu, G. Xu, Y. Zhong, P. Guo, Q. Song, Improving the electrical performance of inverted perovskite solar cell with LiF anode buffer layer, Org. Electron. 101 (2022) 106401, https://doi.org/10.1016/j.orgel.2021.106401.

[31] S. Ijaz, E. Raza, Z. Ahmad, M. Zubair, M.Q. Mehmood, H. Mehmood, Y. Massoud, M.M. Rehman, Numerical simulation to optimize the efficiency of HTM-free perovskite solar cells by ETM engineering, Sol. Energy 250 (2023) 108–118, https://doi.org/10.1016/j.solener.2022.12.027.

[32] T. Minemoto, Y. Kawano, T. Nishimura, J. Chantana, Numerical reproduction of a perovskite solar cell by device simulation considering band gap grading, Opt. Mater. 92 (2019) 60–66, https://doi.org/10.1016/j.optmat.2019.03.048.

[33] E. Raza, Z. Ahmad, F. Aziz, M. Asif, A. Ahmed, K. Riaz, J. Bhadra, N.J. Al-Thani, Numerical simulation analysis towards the effect of charge transport layers electrical properties on cesium based ternary cation perovskite solar cells performance, Sol. Energy 225 (2021) 842–850, https://doi.org/10.1016/j.solener.2021.08.008.

[34] Z. Ahmad, A. Mishra, S.M. Abdulrahim, F. Touati, Electrical equivalent circuit (EEC) based impedance spectroscopy analysis of HTM free perovskite solar cells, J. Electroanal. Chem. 871 (2020), https://doi.org/10.1016/j.jelechem.2020.114294.

[35] A. Mishra, Z. Ahmad, I. Zimmermann, D. Martineau, R.A. Shakoor, F. Touati, K. Riaz, S.A. Al-Muhtaseb, M.K. Nazeeruddin, Effect of annealing temperature on the performance of printable carbon electrodes for perovskite solar cells, Org. Electron. 65 (2019) 375–380, https://doi.org/10.1016/j.orgel.2018.11.046.

[36] M.K. Hossain, G.F.I. Toki, A. Kuddus, M.H.K. Rubel, M.M. Hossain, H. Bencherif, M.F. Rahman, M.R. Islam, M. Mushtaq, An extensive study on multiple ETL and HTL layers to design and simulation of high-performance lead-free CsSnCl3-based perovskite solar cells, Sci. Rep. 13 (2023), https://doi.org/10.1038/s41598-023-28506-2.

[37] P.-C. Kao, C.-T. Chiu, MoO3 as p-type dopant for Alq3-based p–i–n homojunction organic light-emitting diodes, Org. Electron. 26 (2015) 443–450, https://doi.org/10.1016/j.orgel.2015.08.018.

[38] M. Knupfer, H. Peisert, T. Schwieger, Band-gap and correlation effects in the organic semiconductor ${\mathrm{Alq}}_{3}$, Phys. Rev. B 65 (2001) 33204, https://doi.org/10.1103/PhysRevB.65.033204.

[39] J.-H. Kim, Y.R. Kim, J. Kim, C.-M. Oh, I.-W. Hwang, J. Kim, S. Zeiske, T. Ki, S. Kwon, H. Kim, A. Armin, H. Suh, K. Lee, Efficient and stable perovskite solar cells with a high open-circuit voltage over 1.2 V achieved by a dual-side passivation layer, Adv. Mater. 34 (2022) 2205268, https://doi.org/10.1002/adma.202205268.

[40] Y. Tanaka, K. Ikegami, T. Maruyama, H. Kinjo, H. Ishii, Direct observation of charged state in C60-based field-effect transistor using operando photoelectron yield spectroscopy, Appl. Phys. Express. 11 (2018), https://doi.org/10.7567/APEX.11.081601.

[41] S. Zheng, G. Wang, T. Liu, L. Lou, S. Xiao, S. Yang, Materials and structures for the electron transport layer of efficient and stable perovskite solar cells, Sci. China Chem. 62 (2019) 800–809, https://doi.org/10.1007/s11426-019-9469-1.

[42] H.H. Kim, S. Park, Y. Yi, D.I. Son, C. Park, D.K. Hwang, W.K. Choi, Inverted quantum dot light emitting diodes using polyethylenimine ethoxylated modified ZnO, Sci. Rep. 5 (2015), https://doi.org/10.1038/srep08968.

[43] M. Yang, T. Du, X. Zhao, X. Huang, L. Pan, S. Pang, H. Tang, Z. Peng, L. Ye, Y. Deng, M. Sun, C. Duan, F. Huang, Y. Cao, Low-bandgap conjugated polymers based on benzodipyrrolidone with reliable unipolar electron mobility exceeding 1 cm2 V−1 s−1, Sci. China Chem. 64 (2021) 1219–1227, https://doi.org/10.1007/s11426-021-9991-0.

[44] A. Ahmed, K. Riaz, H. Mehmood, T. Tauqeer, Z. Ahmad, Performance optimization of CH3NH3Pb(I1-xBrx)3 based perovskite solar cells by comparing different ETL materials through conduction band offset engineering, Opt. Mater. 105 (2020), https://doi.org/10.1016/j.optmat.2020.109897.

[45] S.R. Hosseini, M. Bahramgour, P. Yardani Sefidi, A. Tabatabaei Mashayekh, A. Moradi, N. Delibas, M.G. Hosseini, A. Niaei, Investigating the effect of non-ideal conditions on the performance of a planar CH3NH3PbI3-based perovskite solar cell through SCAPS-1D simulation, Heliyon 8 (2022) e11471, https://doi.org/10.1016/j.heliyon.2022.e11471.

[46] T. Ouslimane, L. Et-taya, L. Elmaimouni, A. Benami, Impact of absorber layer thickness, defect density, and operating temperature on the performance of MAPbI3 solar cells based on ZnO electron transporting material, Heliyon 7 (2021) e06379, https://doi.org/10.1016/j.heliyon.2021.e06379.

[47] Y.M. Lee, I. Maeng, J. Park, M. Song, J.H. Yun, M.C. Jung, M. Nakamura, Comprehensive understanding and controlling the defect structures: an effective approach for organic-inorganic hybrid perovskite-based solar-cell application, Front. Energy Res. 6 (2018), https://doi.org/10.3389/fenrg.2018.00128.

[48] M. Lazemi, S. Asgharizadeh, S. Bellucci, A computational approach to interface engineering of lead-free CH3NH3SnI3 highly-efficient perovskite solar cells, Phys. Chem. Chem. Phys. 20 (2018) 25683–25692, https://doi.org/10.1039/c8cp03660h.

[49] L. Lin, P. Li, L. Jiang, Z. Kang, Q. Yan, H. Xiong, S. Lien, P. Zhang, Y. Qiu, Boosting efficiency up to 25% for HTL-free carbon-based perovskite solar cells by gradient doping using SCAPS simulation, Sol. Energy 215 (2021) 328–334, https://doi.org/10.1016/j.solener.2020.12.059.

[50] P.K. Patel, Device simulation of highly efficient eco-friendly CH3NH3SnI3 perovskite solar cell, Sci. Rep. 11 (2021) 3082, https://doi.org/10.1038/s41598-021-82817-w.

[51] K.C. Fong, K.R. McIntosh, A.W. Blakers, Accurate series resistance measurement of solar cells, Prog. Photovoltaics 21 (4) (2013) 490–499. http://onlinelibrary.wiley.com/doi/10.1002/pip.1216/full.

[52] R. Singh, S. Sandhu, J.J. Lee, Elucidating the effect of shunt losses on the performance of mesoporous perovskite solar cells, Sol. Energy 193 (2019) 956–961, https://doi.org/10.1016/j.solener.2019.10.018.

[53] Series Resistance | PVEducation, (n.d.). https://www.pveducation.org/pvcdrom/solar-cell-operation/series-resistance (accessed March 28, 2023).

[54] X. Chen, D. Taguchi, T. Manaka, M. Iwamoto, Selective observation of photo-induced electric fields inside different material components in bulk-heterojunction organic solar cell, Appl. Phys. Lett. 104 (2014) 013306, https://doi.org/10.1063/1.4861620.

[55] W. Ming, D. Yang, T. Li, L. Zhang, M.-H. Du, Formation and diffusion of metal impurities in perovskite solar cell material CH3NH3PbI3: implications on solar cell degradation and choice of electrode, Adv. Sci. 5 (2018) 1700662, https://doi.org/10.1002/advs.201700662.

[56] P. Chen, Y. Bai, S. Wang, M. Lyu, J.H. Yun, L. Wang, In situ growth of 2D perovskite capping layer for stable and efficient perovskite solar cells, Adv. Funct. Mater. 28 (2018), https://doi.org/10.1002/adfm.201706923.

[57] S. Bouzenada, A.N. Kaabi, L. Frainkin, T. Salmon, A. Léonard, Experimental comparative study on lithium chloride and calcium chloride desiccants, Procedia Comput. Sci. 83 (2016) 718–725, https://doi.org/10.1016/j.procs.2016.04.159.

[58] D.H. Cao, C.C. Stoumpos, O.K. Farha, J.T. Hupp, M.G. Kanatzidis, 2D homologous perovskites as light-absorbing materials for solar cell applications, J. Am. Chem. Soc. 137 (2015) 7843–7850, https://doi.org/10.1021/jacs.5b03796.

[59] S.N. Habisreutinger, T. Leijtens, G.E. Eperon, S.D. Stranks, R.J. Nicholas, H.J. Snaith, Carbon nanotube/polymer composites as a highly stable hole collection layer in perovskite solar cells, Nano Lett. 14 (2014) 5561–5568, https://doi.org/10.1021/nl501982b.

[60] S. Bai, Z. Wu, X. Wu, Y. Jin, N. Zhao, Z. Chen, Q. Mei, X. Wang, Z. Ye, T. Song, R. Liu, S. Lee, B. Sun, High-performance planar heterojunction perovskite solar cells: preserving long charge carrier diffusion lengths and interfacial engineering, Nano Res. 7 (2014) 1749–1758, https://doi.org/10.1007/s12274-014-0534-8.

[61] Y. Meng, B.R. Magruder, H.W. Hillhouse, On interface recombination, series resistance, and absorber diffusion length in BiI3 solar cells, J. Appl. Phys. 129 (2021), https://doi.org/10.1063/5.0034776.

[62] K.P. McKenna, A.L. Shluger, Electron-trapping polycrystalline materials with negative electron affinity, Nat. Mater. 7 (2008) 859–862, https://doi.org/10.1038/nmat2289.

[63] H.J. Lee, S.I. Na, Investigation of PCBM/ZnO and C60/BCP-based electron transport layer for high-performance p-i-n perovskite solar cells, J. Alloys Compd. 921 (2022), https://doi.org/10.1016/j.jallcom.2022.166007.

[64] P. Szuromi, Improving the performances of perovskite solar cells via modification of electron transport layer, Science 354 (2016), https://doi.org/10.1126/science.354.6309.192-b, 192–192.

[65] K. Lee, J. Ryu, H. Yu, J. Yun, J. Lee, J. Jang, Enhanced efficiency and air-stability of NiO:X-based perovskite solar cells via PCBM electron transport layer modification with Triton X-100, Nanoscale 9 (2017) 16249–16255, https://doi.org/10.1039/c7nr05235a.

[66] M. Méndez, E. Palomares, Alq3 (tris(8-hydroxyquinolinato)aluminium) as a selective n-type contact for FAMAPIBr perovskite solar cells with efficient energy transfer to increase the solar cell photocurrent, RSC Adv. 7 (2017) 35525–35527, https://doi.org/10.1039/c7ra06645g.

[67] Y. Wang, S. Dong, Y. Miao, D. Li, W. Qin, H. Cao, L. Yang, L.L. Li, S. Yin, BCP as additive for solution-processed PCBM electron transport layer in efficient planar heterojunction perovskite solar cells, IEEE J. Photovoltaics 7 (2017) 550–557, https://doi.org/10.1109/JPHOTOV.2017.2651108.

[68] H. Yoon, S.M. Kang, J.K. Lee, M. Choi, Hysteresis-free low-temperature-processed planar perovskite solar cells with 19.1% efficiency, Energy Environ. Sci. 9 (2016) 2262–2266, https://doi.org/10.1039/c6ee01037g.

[69] C. Xu, Y. Zhang, P. Luo, J. Sun, H. Wang, Y.-W. Lu, F. Ding, C. Zhang, J. Hu, Comparative study on TiO2 and C60 electron transport layers for efficient perovskite solar cells, ACS Appl. Energy Mater. 4 (2021) 5543–5553, https://doi.org/10.1021/acsaem.1c00226.

[70] Y. Lin, B. Chen, F. Zhao, X. Zheng, Y. Deng, Y. Shao, Y. Fang, Y. Bai, C. Wang, J. Huang, Matching charge extraction contact for wide-bandgap perovskite solar cells, Adv. Mater. 29 (2017) 1700607, https://doi.org/10.1002/adma.201700607.

[71] F. Wu, T. Chen, X. Yue, L. Zhu, Enhanced photovoltaic performance and reduced hysteresis in perovskite-ICBA-based solar cells, Org. Electron. 58 (2018) 6–11, https://doi.org/10.1016/j.orgel.2018.03.042.

[72] H. Yu, X. Huang, C. Huang, PEIE doped ZnO as a tunable cathode interlayer for efficient polymer solar cells, Appl. Surf. Sci. 470 (2019) 318–330, https://doi.org/10.1016/j.apsusc.2018.11.166.